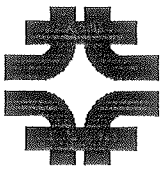

Fermilab

# SSC DETECTOR SOLENOID DESIGN NOTE #109

TITLE: HCD (Hermetic Collider Detector)

AUTHOR: S. Mori, University of Tsukuba, Japan

DATE: Jan 17, 1990

ABSTRACT: This Design Note consists of a 61-page document, dated Jan 4, 1990, received from Shigeki Mori. Some of the material on the magnet appears to be the result of work done by Hitachi, Ltd., under contract to the University of Tsukuba.

January 4, 1990

# HCD (Hermetic Collider Detector)

S. Mori University of Tsukuba

A conceptual design of a large solenoid detector at the SSC has been carried out by a group of physicists mostly from the University of Tsukuba. A 15 m long, thin superconducting solenoid with a bore diameter of 4.5 m provides a uniform axial magnetic field of 1.7 Tesla. The barrel calorimeter is placed outside the solenoid, whereas the endcap calorimeters are placed inside the solenoid. Precision momentum analyses of large-angle muons are performed solely by the central tracking system. Each forward region has a muon spectrometer of magnetized iron toroids. The calorimeter and muon detection systems cover the rapidity range of $\pm$ 3 units. The hermeticity of the calorimetry can adequately be satisfied in the present design.

## 1. INTRODUCTION

The Hermetic Collider Detector, HCD, is a general purpose 4 detector with a thin superconducting solenoid magnet. The design has been carried out primarily at the University of Tsukuba and the design concept is based upon the CDF detector at TEVATRON [1]. The design goal is to satisfy all the basic physics requirements identified by the Large Solenoid Group at Berkeley 87 [2]. The barrel calorimeter is placed outside the solenoid. The most notable disadvantage with this arrangement of CDF-type detectors is that the transition areas between the barrel and endcap calorimeters can damage the hermeticity of the calorimetry. A variety of detector designs have been proposed in order to overcome this drawback [3]. The LSD of Berkeley-87 is one of the most recent detector proposals [2]. Feasibility studies of construction of a large solenoid (8.7 m x 16 m, 2 Tesla) of the LSD were carried out at Tsukuba and at Fermilab [4,5]. It was concluded that construction of such a solenoid is indeed technically feasible. On the other hand,

potential problems associated with cost, on-site fabrication etc. were pointed out.

The HCD has a very long solenoid to improve the hermeticity of the calorimetry at the transition areas. Some advantages of this type of detector were discussed at the Dallas Meeting in June 1989.

In the following section the general characteristics of the HCD is described and in section 3 preliminary results of the conceptual design of the HCD solenoid are presented. In sections 4 and 5 we discuss results of simulation studies on the effects that the solenoid materials cause on the energy resolution and hermeticity of the calorimetry. As an example of the barrel calorimeter a design and cost estimates of the Pb/scintillating fiber calorimetry technique are given in section 6. In section 7 we describe the proposed muon detection system. Conclusions are presented in section 8.

Some of the major subsystems such as the central tracking system and data acquisition system are very common to most designs of large solenoid detectors and are not discussed in this report.

## 2. GENERAL CHARACTERISTICS

The schematic side and end views of the HCD are shown in Figs.2-1 and 2-2. The barrel calorimeter is placed outside of the thin superconducting solenoid of 4.5 m in inner diameter and 15 m in length with a stored energy of 300 MJ. Endcap calorimeters are located inside the two ends of the solenoid. The magnet system with the return yoke arrangement provides a uniform axial magnetic field of 1.7 Tesla at the central tracking system. The most important difference between the HCD and CDF is that the HCD has a very long solenoid in order to satisfy the hermeticity of the calorimetry. The schematic side view of the central section of the CDF is shown in Fig.2-3. The transition region between the barrel and endcap calorimeters at each coil end has a dead area in the the case of CDF. On the other hand, as will be explained later, the HCD is intended to have negligible dead areas for the calorimetry.

The combined material thickness of the barrel calorimeter and return yoke is about 15 $\lambda_0$ at 90 degrees. An iron absorber of 1 m in thickness is used for identification of muons. If punchthrough rates of hadrons are tolerable at the exit of the return yoke, the iron absorber will be removed. Although precision momentum analyses of muons at the barrel section can be made solely by the central tracking system, the iron absorber may be magnetized to aid muon triggering with a rather simple muon tracking system.

In the forward region, $1.5 < |y| < 3.0$, iron toroids of about 8 mTesla are used for momentum analyses of muons.

Weights of the major components are given in Table I. Pb/scintillating fiber calorimeters (Pb/SciFi) are assumed for both the barrel and endcap calorimeters in the weight estimate.

Table I. Weights of the major components of the HCD.

| Component | Weight (metric tons) |
|---|---|
| Calorimeter* | |
| Barrel | 5760 |
| Endcaps | 550 |
| Return yoke | 5620 |
| Muon detector | |
| Barrel absorber (1 m) | 7120 |
| F/B toroids | 11140 |
| Total | 30190 |

*The weights of the Pb/SciFi calorimeters are approximately given by the following relations:

Barrel: $1613\ R + 2129$ (tons)

Endcaps: $120\ R^2 - 57$ (tons)

where R is the bore radius in meters. The above relations hold for the length of the central tracking chamber of 9 m and for the radius R of around 2.25 m.

## 3. HCD SOLENOID

### 3.1 General Characteristics

Successful technical development works have been made in order to fabricate thin, large superconducting solenoids for collider detectors [6]. The HCD solenoid is considerably longer compared with any existing solenoids ever constructed. The stored magnetic energy is also large. On the other hand, the construction method of the HCD solenoid seems to be a rather straightforward extension of the existing technology which has been used successfully in the past.

The main parameters of the HCD solenoid are given in Table II. The mechanical structure is very similar to the CDF solenoid [7]. Fig.3-1 shows the schematic drawing of the end section of the CDF solenoid at the chimney side for illustration. The side view of an axial support is also shown. The solenoid consists of a superconducting coil, an outer support cylinder, a cryostat, a chimney, and a control dewar. The coil can consist of a few modules, each with a coil of a single layer helical winding of aluminum-stabilized NbTi/Cu superconductor and an outer support cylinder. The main parts of the cryostat are a vacuum vessel, a support system, thermal radiation shields, and liquid helium cooling tubes. The forced-flow cooling method of two-phase helium is applied. Table III shows a preliminary study of optimization of the number of modules. The length of a module is a critical parameter if existing facilities should be utilized for fabrication of major components. An arrangement of four modules seems to be advantageous. The cost, construction schedule, and transportation are not serious problems with the HCD solenoid.

The most important requirements for detector magnets at the SSC are stable operation, comfortable safety margin in design, and safety against quenches. The conceptual design of the HCD solenoid is being carried out based upon the above considerations. The safety requirements we impose for the coil during quenches which can be caused by malfunctioning of the refrigeration system, for example, are: (a) the local maximum temperature rise to be less than 100 K and (b) the maximum voltage to be less than 1000 V. The maximum voltage appears

across the protection resistor immediately after the quench protection circuit is activated. The voltage rise due to the resistivity of the normal section of the coil during a quench is generally small. Therefore, when the protection resistor is grounded at the middle, the maximum voltage to ground is less than 500 V under the present requirements. The maximum temperature rise limit is primarily determined from considerations of mechanical stresses caused by the thermal gradient in the coil and recovery times after quenches. The thermal expansion rates are relatively small below 100 K [8]. It should be noted that temperature rises above 100 K do not necessarily mean any damages to the solenoid as long as the temperature gradient in the cold mass is tolerable. Longer recovery times can hurt physics runs if they occur frequently.

Extensive analyses of deflections and stresses in the yoke due to electromagnetic loadings and structural weight were performed in the case of the CDF solenoid [9]. The return yoke arrangement of the HCD solenoid is much simpler compared with that of the CDF solenoid. Therefore, we do not anticipate any serious problems, but the structural concern is one of the main reasons why we choose the magnetic field of 1.7 Tesla. Detailed studies on structural analyses will be made soon.

### 3.2 Conductor

The design parameters of the aluminum-stabilized NbTi/Cu superconductor are given in Table IV. Instead of a monolithic superconductor used in the CDF solenoid [10],a stranded cable of 8 to 10 conductors will be used in order to eliminate the possibility of having broken conductors due to inclusions and also to produce conductors with longer unit lengths. The unit length is estimated to be 5.5 to 8 km for the diameter of the base conductor of 1.1 mm which seems to be a technical limit at present. Since the overall length of the conductor is about 35 km, the number of conductor joints in a module can be one in a 4-module arrangement. Further optimization will be continued in this regard. Fig.3-2 shows the designed short-sample magnetic flux versus critical current relation and the load line. The local maximum field is estimated to be about 2 Tesla.

The conductor height of 28 mm is determined primarily from

the requirements for quench properties estimated by the hot spot model. In this model the relation between the maximum temperature rise at the hot spot, $T_{max}$, and the maximum voltage, $V_{max}$, is given by

$$\gamma \int^{T_{max}} \frac{C}{\rho}\, dT = \frac{E_0\, J_0^{\,2}}{V_{max}\, I_0} = \Gamma \qquad (1)$$

where $\gamma$, C, and $\rho$ are respectively the density, specific heat, and resistivity of the conductor, the variable T is temperature, $I_0$ and $J_0$ are respectively the coil excitation current and current density, given by $J_0 = I_0/A$, A being the conductor cross section area, and $E_0$ is the coil stored energy, given by $E_0 = L\, I_0^{\,2}/2$, L being the coil inductance. The parameter $\Gamma$ depends upon $T_{max}$ and the characteristics of the conductor and is estimated to be approximately $1 \times 10^9$ ($A^2s/cm^4$) for $T_{max}$ = 100 K. Fig.3-3 shows the relation between $\Gamma$ and $T_{max}$ for aluminum with RRR = 2450 (residual resistivity ratio). For $V_{max}$ = 1000 V Eq. (1) yields the following relations:

$$E_0 J_0^{\,2} (JA^2/m^4) = 1 \times 10^{20}\ I_0(A) = 8 \times 10^{23}$$

$$J_0 = 51.6\ (A/mm^2).$$

Thus we have S = 8000/51.6 = 155 = 5.68(W) x 27.3(H) ($mm^2$) and we choose temporarily the conductor height of 28 mm. The width of 5.68 mm is uniquely determined by the design parameters of the magnetic flux (1.7 Tesla) and excitation current (8000 A). The hot spot model gives very conservative limits as long as the protection circuit is operational.

As can be seen from Eq. (1), for a given current density $J_0$ the hot spot model favors higher excitation current to lower the maximum voltage during a quench. The stored energy can be dumped into the protection resistor much faster because the inductance of the solenoid is smaller. On the other hand, heat dissipation at conductor joints increases proportionally to $I_0^{\,2}$ and thermal leaks at power leads of typical designs increase almost proportionally to $I_0$. The estimated heat loads at conductor joints and power leads are respectively 3 and 23 W at $I_0$ = 10000 A, and 6 and 34 W at $I_0$ = 15000 A. Although these

figures at 10000 A, for example, are not necessarily formidable, we proposed the excitation current of 8000 A. We must also consider the cost of a power supply system.

As demonstrated by computer simulations in the case of the CDF solenoid, the Joule heat due to eddy currents induced inside the solenoid support cylinder during a quench causes the quench-back phenomenon [11]. As a result the entire coil becomes normal within a few seconds. The inductance and resistance in the direction of the coil circumference of the support cylinder of the HCD solenoid are estimated to be 1.7 μH and 2.3 μΩ, respectively. Then the induced current in the support cylinder is given approximately by $1.9 \times 10^5 \exp(-t/75)$ A for a protection resistor of 0.125 Ω (t: time after a quench in seconds) and the Joule power is about 80 kW immediately after the protection circuit is activated. Therefore, the entire HCD solenoid quenches immediately due to the quench-back effect. In such cases the temperature rise should be uniform and substantially lower than the maximum temperature rise of 100 K estimated by the hot spot model.

In case the stored energy is completely absorbed inside the solenoid, a uniform temperature rise of the cold mass of 24 t reaches about 83 K. A temperature rise of 100 K from liquid helium temperature corresponds to an enthalpy of about 17 J/g. This implies that the stored energy of 300 MJ is equivalent to a uniform temperature rise of 100 K in a cold mass of about 18 t. Therefore, if the temperature gradient in the cold mass is small during a quench, the conductor height can be safely reduced.

We will investigate an emergency case in which the quench protection circuit fails to operate. Since such cases seem to be extremely rare to happen, we may safely relax the limit of temperature rises above 100 K. Detailed computer simulation studies which take into account failures of the quench protection system and simultaneously the quench-back effects will be carried out in order to estimate temperature distributions inside the coil during quenches. The conductor height will be optimized further.

Extensive computer simulations were carried out in the case of the CDF solenoid. The maximum temperature rise was

estimated to be about 180 K in case the protection circuit failed completely [11]. In the normal case in which the protection circuit is operational, the temperature rises at the coil and support cylinder are estimated to be respectively about 80 and 40 K in about 15 s after a quench and both temperatures become equalized at 70 K in about 10 m. We believe that even a temperature rise of 180 K in a very rare emergency case is safe for the coil.

The eddy current power loss in the coil, $P_{coil}$, during charging time can be estimated by the relation [7,12]:

$$P_{coil} = N_t \frac{1}{R_c} \left(A_{eff} \frac{dB}{dt}\right)^2$$

where N is the number of turns, $R_c$ the effective resistance of one turn, and $A_{eff}$ the effective conductor area of magnetic flux crossing per turn. For the HCD solenoid we have $N \cong 2540$, $R_c \cong 3.8 \times 10^{-6}$ Ω, and $A_{eff} \cong 0.10$ m$^2$. Therefore, for the charging time of 30 minutes we get $P_{coil} \cong 6$ W. As will be discussed in the following section, the Joule heating due to eddy currents in the support cylinder during charging time can be a more serious limiting factor for the charging speed of the solenoid.

### 3.3 Support Cylinder and Module Connection

The outer support cylinder supports the radial magnetic force, $P = B^2/2\mu_0 = 0.117$ (kg/mm$^2$) at 1.7 Tesla together with the coil. In the HCD solenoid the support cylinder made of A2219-T851 aluminum alloy is designed to support essentially the total radial magnetic force. The axial magnetic force is negligibly small in the HCD solenoid [13]. We note that the accumulative axial comppressive force from one side of the coil is estimated to be about 150 metric tons in the normal arrangement with the return yoke. Appreciable axial forces exist at the two ends of the coil and less significantly at the module joints. The allowed stress of this alloy $\sigma_{al}$ is 22.7 kg/mm$^2$ at 4.2 K ($\sigma_{al} = \mathrm{Min}(\sigma_u/3, 2\sigma_y/3)$; $\sigma_u = 68$ kg/mm$^2$, $\sigma_y = 44$ kg/mm$^2$ at 4.2 K). The hoop stress at the support cylinder is given by

$$\sigma = PR/t = 0.117 \times 2380/t = 278/t \ (kg/mm^2)$$

where R and t are the radius and thickness of the support cylinder, respectively. Therefore, we have

$$t > 278/\sigma_{al} = 278/22.7 = 12.2 \ (mm).$$

Thus we choose the support cylinder thickness of 14 mm.

A schematic drawing of one of the solenoid end sections is shown in Fig.3-4(a). The support cylinder is made thicker in order to increase the mechanical rigidity for the radial or/and axial support systems, as can be seen in Fig.3-1. The axial decentering force $F_z$ is estimated to be less than 73 t. (See section 3.5.) For r = 2380 mm and h = 16 mm we have the minimum value of $l_1$ to be 9.3 mm for 120 M12 support bolts. A horizontal bolt hole shown in the figure is for the bolts to provide the axial preload to the coil. Fig.3-4(b) shows the schematic drawing of an end section of the coil module. This side is used for connection of two modules. At the other coil end of a module which is not shown in Fig.3-4(b) the space and SUS plate between the end ring and insulator can be eliminated. Thus, the width of the dead space can be reduced to 24 mm at this end.

As mentioned in section 3.1, the module length in a two module arrangement can be a serious limitation for existing facilities. A fabrication technique of 7.5 m long support cylinders is being investigated.

The charging time of the solenoid is limited mainly by the eddy current induced circumferentially on the support cylinder. The Joule heating power due to this induction current, P, is given by

$$P = (M \, dI/dt)^2/R$$

where R is the resistance of the support cylinder in the circumferential direction given in the previous section, M is the mutual inductance between the coil and support cylinder, and dI/dt is the charging rate. M is estimated to be 3.9 mH. For P = 100 W we have dI/dt = 3.9 A/s. Therefore, the charging

time for the excitation current of 8000 A will be 34 minutes and the charging voltage of the power supply will be 9.4(H) x 3.9(A/s) = 37 V. If a shorter charging time is required, higher cooling power is needed during the charging time, or a special arrangement in the support cylinder to increase the resistance of the support cylinder, R, must be made. As discussed in the previous section, eddy currents in the support cylinder are very beneficial in helping uniform temperature rises in the coil by the quench-back effect during quenches and also the eddy current power loss in the coil must be taken into account.

3.4 Vacuum Chamber

The thickness of the outer vacuum chamber is determined by the critical pressure at which buckling occurs. The critical pressure is given by

$$P_k = 0.807 \frac{E}{(1-\nu^2)^{3/4}} \frac{t^{5/2}}{LR^{3/2}}$$

$$= 3.05 \times 10^{-6} t^{5/2}$$

where L, R, and t are respectively the length, radius, and thickness of the outer vacuum cylinder, and E = 7200 kg/mm$^2$ and $\nu$ = 0.3 for aluminum alloy, A5083. For the safety factor SF = $P_k/P$ = 3 and P = 0.01033 kg/mm$^2$ we have t = 40 mm. The hoop stress of the outer vacuum cylinder is $\sigma$ = PR/t = 0.01033 x 2650/40 = 0.7 (kg/mm$^2$) < $\sigma_{al}$ = 10.3 (kg/mm$^2$) for A5083.

As will be discussed in the following section, the effective material thickness of the solenoid seen from the interaction point is inversely proportional to sin $\theta$, where $\theta$ is the polar angle. Thus the solenoid material around the calorimeter transition areas, about 6 m from the interaction point in the axial direction, becomes effectively 2.5 times thicker than that at 90 degrees. We propose to use aluminum honeycomb structure instead of aluminum plate material for the outer vacuum cylinder in the axial distance from 4 to 6 m. The physical thickness of the honeycomb structure is about 75 mm and its material thickness is about 0.13 $X_0$ (radiation length). This large physical thickness of the honeycomb cylinder does

not cause any spatial problems since the honeycomb sections are away from the solenoid ends where many structual materials such as the coil support system are very tightly packed.

Fabrication of a honeycomb cylinder of about 5 m in diameter and 2 m in length as a single unit may require a new facility [14]. Instead we propose an alternative fabrication method in which a cylinder is formed by welding four quadrants. Fig.3-5(a) illustrates the fabrication procedure. A quadrant section can be processed in an available oven facility. Welding of quadrants must be done under a proper cooling condition. The side view of the honeycomb vacuum wall is shown in Fig.3-5(b). Aluminum inner supporting plates of honeycomb cores will be assembled by welding to provide good vacuum seals. Detailed studies on the fabrication procedure and optimization of parameters are being carried out.

The thickness of the inner vacuum cylinder, 7 mm, is made thicker than the code requirement in order to give a comfortable safety margin for the installation of detectors inside the coil

The radial deformations of the vacuum chamber under vacuum can be estimated by using the following relation:

$$\Delta R = PR^2(1 - \nu/2)/Et$$

where $P = 0.01033$ kg/mm$^2$, $\nu = 0.3$, and $E = 7200$ kg/mm$^2$. Therefore, the deformations of the inner and outer vacuum cylinders of 40 and 7 mm in thickness are respectively 0.21 and 0.89 mm.

## 3.5 Support System

The coil support system holds the weight of the cold mass and axial and radial decentering forces due to magnetic forces. Thermal leaks from the cryostat at room temperature to the cold mass at liquid helium temperature through the support system must be kept reasonably small. The decentering forces are estimated to be 3.7 and 2.6 t/mm in the axial and radial directions, respectively. If we assume a maximum displacement of 20 mm for the solenoid from the ideal magnetic center, the maximum loads due to magnetic forces are 73 and 53 t in the axial and radial directions, respectively and they are about

twice of those of the CDF solenoid.

Various ideas for the coil support system for the HCD solenoid are being investigated. A CDF-type support system is a good candidate. The schematic diagram of the radial and axial support system of the CDF solenoid is shown in Fig.3-6. It consists of 6 axial and 24 radial supports. All the axial supports are placed at the chimney end of the coil, whereas six pairs of 12 radial supports are placed at each end. This arrangement allows nearly freely thermal contraction of the coil, about 20 and 6 mm in the axial and radial directions, respectively, when the coil is cooled from room temperature to liquid helium temperature. A spherical bearing at each end of a support is used to reduce the stress due to the thermal contraction. The schematic section view of the CDF radial support is shown in Fig.3-7. (See Fig.3-1 for the axial support.)

The coil support system of the HCD solenoid must take twice larger loads and handle larger thermal contraction, about 60 and 10 mm in the axial and radial directions, respectively, compared with that of the CDF solenoid. The axial support system is relatively easy to design. If we choose the inner and outer diameters of a main cylinder of an axial support made of Inconel 718 to be respectively 30 and 40 mm, then the maximum stress of the cylinder is 22 $kg/mm^2$. (The yielding and ultimate stresses of Inconel 718 are 106 and 130 $kg/mm^2$, respectively.) The buckling stress of the main cylinder is estimated to be 92 $kg/mm^2$ by using a parabolic formula for the cylinder length of 400 mm. Thus the safety factor is obtained to be 92/22 = 4.2 which is acceptable.

The maximum prime load for a radial support rod is estimated to be 11.1 t. Therefore, for a rod of 30 mm in diameter the maximum prime stress is 15.7 $kg/mm^2$, which is appreciably smaller than the allowable stress of 43.4 $kg/mm^2$. The differential thermal stress of the radial supports can be reduced substantially by tilting the rods by about 10 degrees at room temperature. Thus, when it is cooled to liquid helium temperature, the thermal stress can be a reasonable value of 14 $kg/mm^2$ for the rod length of 590 mm. Therefore, the sum of the primary and secondary stresses of the radial supports in the

present design is about 30 $kg/mm^2$ for an allowed stress of 130 $kg/mm^2$.

The parameters of the axial and radial supports given above can satisfy requirements for mechanical strengths. Detailed design work including housings of spherical bearings and thermal intercepts must be made. For example, in a breaking test of an axial support sample of the CDF solenoid the housing of the spherical bearing broke and no damages to the other parts were observed. Further optimization including heat loads through the support system will be carried out.

### 3.6 Material Thickness

Table V lists the material thicknesses of various solenoid components in physical lengths and in radiation lengths in the radial direction of the coil. The second values given for the outer vacuum cylinder correspond to the honeycomb arrangement. The total material thickness is 1.18 and 0.862 $X_0$ for solid aluminum and honeycomb structure used for the outer vacuum cylinder, respectively. Fig.3-8 shows the effective material thickness of the HCD solenoid seen from the interaction region as a function of the axial distance. The honeycomb arrangement in the radial distance from 4 to 6 m helps keep the material thickness below 2.4 $X_0$ in the entire section.

As mentioned earlier, the conductor dimension has not been fully optimized. We may be able to reduce the height by as much as 0.03 $X_0$ after careful simulation studies. The honeycomb section can be extended longer if it is seriously desired.

## 4. EFFECTS ON CALORIMETER PERFORMANCE DUE TO COIL MATERIALS

Materials in front of a shower counter generally degrade the energy resolution and pion rejection factor of the counter. It is very important to study quantitatively how much effects the coil materials cause on the energy resolution of the barrel calorimeter in the HCD. Fig.4-1 shows results of computer simulations for the energy loss of the electron in an aluminum absorber as a function of the electron energy. The GEANT program was used in these simulations. The solid curves represent the

energy losses for various absorber thicknesses from 1 to 4 $X_0$. The dashed curves show the fraction of the incident energy in per cent corresponding to the energy loss. The dashed curves are always steeper than the solid curves at the crossing points. This implies that the fractional energy losses are larger at lower incident energies. A 100-GeV electron loses on average about 1% of the incident energy in an absorber of 2 $X_0$.

The most important factor that determines the energy resolution is the rms fluctuation of the energy loss inside the absorber. It should be pointed out that the average energy loss can be corrected by energy calibration data. Fig.4-2 shows calculated rms energy losses of electrons in aluminum absorbers as a function of the electron energy. The solid and dashed curves represent respectively the rms energy loss and the fraction of the incident energy corresponding to the rms energy loss. The rms energy loss of a 100-GeV electron in an aluminum absorber of 2 $X_0$ is about 0.5 GeV or 0.5% of the incident energy. In the electron energy range above 40 GeV the rms energy loss in an aluminum absorber of 2 $X_0$ is less than 1% of the incident energy. The rms energy losses become less important with increasing electron energies.

Calculated fractional rms values of the energy loss are replotted in Fig.4-3 as a function of the aluminum absorber thickness for various incident electron energies from 10 to 200 GeV. This plot is easily compared with experimental data measured by the CDF group in the electron energy range between 25 and 150 GeV, shown in Fig.4-4 [15]. The measured data indicate that the energy resolution becomes constant for absorbers of less than 2 $X_0$ in the electron energy range above 50 GeV. The overall energy resolution is determined by the quadratic sum of the energy resolution without any absorber and the rms fluctuation of the energy loss in the absorber. Since the rms energy loss in an absorber of 2 $X_0$ is about 1.2% at 25 GeV (Fig.4-3), the contribution from the absorber seems to be still noticeable.

Figure 4-5 shows the energy resolution of an SF03 lead glass counter (18 $X_0$) measured with aluminum absorbers with different thicknesses in front [16]. Above 16 GeV the energy resolution is not significantly degraded by aluminum absorbers thinner than 2 $X_0$. The experimental data shown in Figs.4-4 and

4-5 are quite consistent with the present simulation results.

It can be concluded that the materials of the HCD solenoid in front of the barrel calorimeter will not degrade experimental data at the SSC at any significant level.

Electron identification can be provided by calorimetry and recent experimental results on the $\pi/e$ separation using EM calorimeters are summarized in the Task Force Report on Detector R&D for the SSC [17]. Since the development of electron cascade showers in matter is substantially different from that of hadronic showers, this property has been used to identify an electron. Common techniques used are: (1) comparison of the EM shower energy with the momentum, (2) ratio of shower energies in EM and hadron calorimeters, (3) ratio of the front end energy to the total shower energy in an EM calorimeter, and (4) measurement of the lateral shower profile near the shower maximum.

The amount of material in front of an EM calorimeter can degrade the pion rejection factor. In techniques (1) and (2) the degraded energy resolution directly influences the rejection factor, but it should be negligible at higher energies. The rejection factor in technique (3) depends upon details of longitudinal segmentation in the EM calorimeter and does not seem to be sensitive to a small amount of absorber material. Technique (4) is clearly insensitive to the absorber in front.

Pions which have zero prong interactions such as $\pi^- p \rightarrow \pi^0 n$ in the upstream region of the EM calorimeter are likely to be misidentified as electrons. The chance for a zero prong event is proportional to the material thickness and is estimated to be $10^{-3}$ in an aluminum absorber of 1 $X_0$ at 30 GeV [18]. This should give a rough indication of the pion survival rate.

## 5. CALORIMETER HERMETICITY AT TRANSITION AREAS

One of the major concerns of CDF-type detectors is the hermeticity of the calorimetry at the transition areas between the barrel and endcap calorimeters. In this section we demonstrate that the arrangement of the solenoid and calorimetry in the HCD provides excellent hermeticity of the calorimetry. This is the main reason why the proposed detector is named "HCD".

Figure 5-1(a) shows the solenoid system and the barrel and endcap calorimeters. Details of the calorimeters made of scintillating fiber/lead modules will be described later. The transition area near y = 1.6 can be simulated by a simple model shown in Fig. 5-1(b). The corner of the endcap calorimeter has a bevelled edge parallel to the particle trajectory originated from the interaction region. The longitudinal dimension of the endcap calorimeter is assumed to be 50 cm, but it is clear that this dimension is not critical as long as it can contain electromagnetic cascade showers sufficiently in the longitudinal direction. In the present calculations which use the GEANT 3 program the solenoid is replaced by an aluminum absorber of 3 $X_0$ in thickness. It should be noted that, as shown in Fig.3-8, the thickness of the solenoid in the present design with honeycomb outer vacuum walls is about 2.2 $X_0$ near y = 1.6. The endcap calorimeter has a frame absorber at the edge. The active calorimeter volumes of the barrel and endcap calorimeters are substituted by lead blocks with the reduced density of 80% of normal lead. This simulates scintillating fiber/lead calorimeters with a volume ratio of 1:4. The beam angle with respect to the edge is denoted .

Figure 5-2 shows the average deposition energy distributions calculated in the coil and the barrel and endcap calorimeters for 20-GeV electrons as a function of the displacement from the edge (x). Unless stated otherwise, the electron is incident in the direction parallel to the edge ($\theta = 0°$) and distributed uniformly in the x direction throughout this section. In this calculation the thickness of the frame absorber at the edge of the endcap calorimeter is assumed to be zero and also the calorimeters are replaced by lead blocks with normal density. The energy absorption by the aluminum absorber (coil) of 3 $X_0$ is about 30% at the peak and about 5% at x = 0.4 cm. The dimension of 0.4 cm corresponds to the rapidity interval of about 0.002. Therefore, as long as non-active frame materials at the edge of the endcap calorimeter are negligible, effects on the hermeticity of the calorimeter due to the coil material can be regarded very small in this geometry. We note that electrons which do not strike the endcap calorimeter (x < 0) lose about 2 GeV in the coil as discussed in the previous

section. It must be pointed out that the energy calibration of both the barrel and endcap calorimeters in the combined geometry is very important at the transition area in order to get correct energy information for incident electrons.

The frame material of the endcap calorimeter at the edge can be very critical to the hermeticity of the calorimeter due to energy absorption by the frame itself and also due to electromagnetic shower development at the coil induced by the frame. Figs.5-3(a) and (b) show the average energy deposition distributions in the barrel and endcap calorimeters, the "coil", and the frames of 2 cm thick aluminum and 1 cm thick iron. 20-GeV electrons are incident parallel to the frame edge. In the case of the aluminum frame the energy absorption in the coil section is larger than in the frame and the sum of the deposited energies in the calorimeters (B + EC) is about 50% of the incident energy in the area with almost the same width as the frame thickness. The combined energy resolution for the calorimeters in this area will be degraded, but limited information will still be attainable if sufficient calibration data are available. On the other hand, in the case of the iron frame the energy absorption in the iron frame is very large and the sum of the energies deposited in the calorimeters is as low as 15% in the area behind the frame. The energy absorption in the coil itself is rather small because the iron frame absorbs a large fraction of the incident energy. The calorimeter frame of heavy elements always causes serious problems to the hermeticity of the calorimetry in any detector geometry regardless of the coil arrangement. It seems to be very difficult to measure electron energies in this shadow region.

Figure 5-4 shows the fractional energy deposition at x = 1 cm in each section as a function of the incident electron energy in the case of the 2 cm aluminum frame. The energy sum deposited in the calorimeters is about 50% and almost independent of the incident energy. The energy deposition rate in the barrel calorimeter increases at higher energies.

Figures 5-5(a) through (d) show the average energy deposition distributions for 20-GeV electrons in the 2 cm aluminum frame for $\theta = 0°$, $5°$, $3°$, and $-3°$, in this order. The aluminum frame is located in the region between x = 0 and 2 cm as

indicated in the figures. The energy sum deposited in the calorimeters is appreciably higher in the cases of larger incident angles compared with that in the case of $\theta = 0°$, but the general tendencies are more or less similar. The energy absorption rate by the aluminum frame becomes smaller with increasing incident angles because the effective frame material in the longitudinal direction becomes less.

The average energy deposition distributions for 20-GeV electrons in the case of the 1 cm iron frame are shown in Figs. 5-6(a) and (b) for $\theta = 0°$ and 5°. The distributions for $\theta = 0°$ are again shown for comparison. The energy loss in the iron frame is dominant in both cases. At $\theta = 5°$ the energy absorption rate by the iron frame is almost 50% in the x interval of about 4 cm.

It can be concluded that the frame structure of the endcap calorimeter is very critical to the hermeticity of the calorimetry of the detector. Materials of lighter elements such as aluminum alloy are very desirable as the frame material. The fractional energy loss outside the calorimeters is less than 50% and the loss area is limited to the projected area with the dimension similar to the frame thickness. On the other hand, the iron frame of the endcap calorimeter seems to be very harmful.

In the present studies the longitudinal dimension of the endcap calorimeter was assumed to be 50 cm (Fig.5-1(b)). As pointed out before, this dimension can be adjusted to give enough space between the solenoid and the endcap calorimeter without sacrificing the hermeticity of the calorimetry. This space can be utilized for cabling for the inner tracking system and for other devices installed in the inner central area. Furthermore, as seen from Fig.5-1(a), the two end sections of the solenoid which always have heavy structures (Fig.3-1) are completely hidden behind the endcap calorimeters. The chimney can be arranged to give minimum interference with the barrel calorimeter.

# 6. CALORIMETRY

## 6.1 General

The barrel calorimeter of the HCD can be any one of the following techniques: scintillating fiber (or tile) calorimetry, warm liquid calorimetry, and liquid argon calorimetry. We choose lead/scintillating fiber calorimetry as the first candidate for the barrel calorimeter. Some of advantages of this calorimetry are: (a) fast time response, (b) good energy resolution, (c) reasonable hermeticity, (d) flexible transverse segmentation, (e) good mechanical stability, and (f) easy construction. In the barrel section with zero magnetic field photomultiplier readout is readily available. Potential disadvantages are problems associated with (a) radiation damage, (b) longitudinal segmentation, (c) calibration, and (d) cost.

In the endcap sections the best choice is not finalized yet. Problems associated with radiation damage, readout in a magnetic field of 1.7 Tesla, and structural material must be solved. As discussed in the previous section, materials in a support frame such as a stainless steel cryostat can have very serious effects on the hermeticity. Considerable R&D is needed to find the best solution.

In this section we describe a design of the barrel calorimeter which employs conventional scintillating fibers made of SCSN38 and photomultiplier tube readout. Extensive studies on plastic scintillating fibers and plastic scintillating fiber calorimetry have been carried out at KEK [19]. A design effort for a novel calorimetry technique, an "RGB" calorimeter, is being carried out and it will be described elsewhere. In this new calorimeter two fibers, R3 and SCSN81, are glued to form a single fiber and a group of these fibers are imbedded in a lead absorber in the longitudinal direction. The fiber arrangement is similar to the "spaghetti" calorimeter proposed by P. Jenny et al.[20] R3 and SCSN81 fibers used in the EM and hadron sections emit red and green lights, respectively. Red and green lights are read separately by an arrangement of filter and wavelength shifter to provide longitudinal segmentation.

The side and end views of the barrel calorimeter with transverse segmentation of $\Delta\eta = 0.04$ and $\Delta\phi = 0.04$ are shown in

Fig.5-1(a) and Fig.6-1, respectively. The main parameters of the barrel calorimeter are given in Table VI. The calorimeter is composed of 13440 modules to form a tower geometry. Each module consists of EM and hadron sections. The total weights of the EM and hadron sections are estimated to be respectively 690 and 5070 metric tons. The volume ratio of Pb:SciFi is 4:1 in both sections in order to achieve the optimal e/$\pi$ response [21].

6.2 Barrel EM Calorimeter

An EM section has two longitudinal segmentations. Scintillating fibers of 1 mm in diameter are embedded in lead absorbers in the direction transverse to the incident particle. Fig.6-2 shows the schematic drawing of the EM section of a module. In the two sections fibers are arranged in the horizontal and vertical directions. Scintillation lights are collected through wavelength shifter plates at the two ends. The arrangement of the EM calorimeter is very similar to sampling scintillator-tile calorimeters such as those of the CDF and ZEUS detectors [1,22].

In Fig.6-2 we show an option in which each section is divided into two subsections in the readout system. Lights from a pair of wavelength shifter plates in each subsection are combined together at a photomultiplier tube. Thus we have 2 by 2 transverse segmentations in one module. If desired, much finer transverse segmentations in this mode are feasible in readout. Light guide plates, plastic fibers, and photomultiplier tubes form the light readout system. In the present design two longitudinal segmentations in the EM calorimeter is maximum. R&D work is being carried out to study various properties in this proposed arrangement which include light yield, homogeneity of light collection efficiency along the fiber axis, and response at the outer edges of a module where wavelength shifter plates and the outer frame of the module container are placed.

It is well known that the energy resolution of an EM spaghetti calorimeter depends on the angle between the beam and fiber axis. It becomes rapidly poorer at angles less than about 2 degrees due to the so-called channelling effect. Since the present transverse fiber arrangement is free from the channell-

ing effect, the energy resolution is optimal.

6.3 Barrel Hadron Calorimeter

The hadron calorimeter uses scintillating fibers of 2 mm in diameter in order to reduce fiber cost. Fig.6-3 shows the energy resolution for compensating Pb/scintillator calorimeters as a function of the fiber diameter (or scintillator plate thickness) [23]. We believe that the energy resolution of $\sigma/E = 0.38\ E^{1/2}(GeV^{1/2})$ for the barrel hadron calorimeter is sufficiently good. Fibers are arranged in the same manner as in a typical spaghetti calorimeter and lights are collected directly on photomultiplier tubes at the downstream end. Finer transverse segmentation in a hadron module is very flexible. No longitudinal segmentation is planned.

6.4 Radiation Damage

It should be pointed out that radiation damage problems with the EM and hadron calorimeters are less serious in the present design. Since the length of a typical scintillating fiber in an EM module is about 10 cm, the light attenuation is negligible. Also, radiation dose rate at the barrel hadron calorimeter is expected to be modest.

6.5 Cost

The total cost of the calorimeter system is mainly determined by material cost, construction labor cost, and readout electronics. The material cost includes scintillating fibers, wavelength shifter/light guide materials, photomultiplier tubes/power supplies, and lead absorber materials. Table VII lists estimated costs of the major components. The cost of a scintillating fiber is estimated to be proportional to the diameter of the fiber. Therefore, the total fiber cost of the compensating barrel calorimeter is inversely proportional to the fiber diameter. This is the main reason why we propose to use 2 mm fibers in the hadron calorimeter. In the table we assumed that the cost reduction rate due to an order of a large quantity is 2/3. The overall material cost without including readout electronics is estimated to be $69 \times 10^8$ yen (JFY89).

Table VIII shows estimated costs for combinations of

various alternatives regarding the fiber diameter in the hadron calorimeter and the transverse segmentation. The fiber diameter and subsegmentation in the EM section are assumed to be 1 mm and 2 x 2, respectively.

We guess the construction labor cost to be similar to the material cost given in the tables.

## 7. MUON IDENTIFICATION AND MOMENTUM MEASUREMENT

We propose a simple muon detection system in the central region. Momentum measurements of large-angle muons will be performed by the central tracking system and no precision measurement will be attempted by magnetized iron toroids in the central region. If we use a central tracking system similar to that proposed in the LSD, Berkeley 87 [2], the $BL^2$ factor alone improves the momentum resolution of the HCD by a factor of about 2. The central tracking system should have a momentum resolution of 0.3 $p_T$(TeV/c) or better in order to be able to make sign selection of a 1 TeV muon. As can be seen easily from Fig. 13 in the report of the LSD group, no iron toroid system can compete with the central tracking system for better momentum resolution. Redundant momentum measurement of muons is always desirable in order to reduce background contributions. It must, however, be realized that any toroid system becomes very massive and expensive in order to be redundant regarding the momentum analysis.

In the forward regions muons are momentum analyzed by magnetized iron toroids of about 8 mTesla as shown in Fig.2-1. The muon tracking system should be designed to provide a momentum resolution of 0.1 + 0.1 $p_T$(TeV/c). The forward muon system together with the central muon detection system provides the rapidity coverage of up to $\pm$ 3 which satisfies some of physics requirements such as the Higgs reconstruction efficiency [24].

The combined material thickness of the barrel calorimeter and return yoke is at least 2.7 m of iron equivalent or 15 $\lambda_0$. This thickness can be marginal regarding punchthrough rates. In Fig.2-1 an iron absorber of 1 m in thickness is added to reduce punchthrough rates. Briefly we will study the feasibility of a

CDF-type muon trigger system in the HCD. Fig.7-1(a) shows the relation between the radius and deflection angle of a 50 GeV muon at 90 degrees. The energy loss in the materials is neglected. At the exit of the muon identifier the deflection angle is 19 mrad in the azimuthal angle and the rms multiple Coulomb scattering angle is 5.7 mrad. Therefore, a measurement of the exit azimuthal angle of a muon can provide the capability of momentum selection of the muon at the level of 3 standard deviations. It must be emphasized that this clean separation is possible because the cancellation of the deflection angle by the return yoke is small in the HCD. Return flux is confined in the thin yoke of 70 cm in thickness. At smaller angles separation becomes slightly poorer due to larger multiple Coulomb scattering angles. The degree of confusion due to Coulomb scattering is energy independent as long as the energy loss can be neglected. Fig.7-1(b) shows a schematic drawing of a 1st or 2nd level muon trigger system. For modest tracking parameters, $\sigma_x$ = 1.5 mm and d = 30 cm, we get the angular resolution of 7 mrad. Thus, a trigger such as $p_T$ > 50 GeV/c can be made relatively easily for a clean muon track.

The 1 m iron absorber can be magnetized in the circumferential direction. The polar angle deflection is 12 mrad in a magnetic field of 2 Tesla and can be used as an additional muon trigger.

## 8. CONCLUSIONS

We demonstrated that the HCD is indeed reasonably hermetic. The HCD solenoid is very practical in regard to design safety, construction schedule, and cost. There are no unknown technical questions to be answered. Construction will be simple extension of the existing technology. The material thickness of the solenoid is designed to be 0.86 $X_0$ in the axial distance between 4 and 6 m from the coil center by using honeycomb outer vacuum walls. This arrangement allows us to keep the effective material thickness of the solenoid seen from the interaction region less than 2.2 $X_0$ for the entire coverage. Thus we could prove that the coil materials in front of the barrel calorimeter

are not serious limitations at the SSC regarding the energy resolution and e/π separation.

Although a crack between the barrel and endcap calorimeters appears to be large from the cross sectional view, particles produced at the interaction area see very small inactive areas when the endcap calorimeter is designed with a proper bevelled edge. If an inactive support frame at the bevelled edge is made of steel, it can cause significant energy losses for electrons. If an aluminum frame is used, the sum of energies deposited in the support and solenoid is less than 50% and useful energy information of incident electrons can be obtained with a slightly degraded energy resolution. Energy loss patterns depend strongly upon the incident angle of an electron with respect to the bevelled edge, but the fractional energy loss in the inactive materials seems to be independent of the incident electron energy.

Access to the central tracking system (cabling etc.) can be made between the solenoid and endcap calorimeter and through holes in the return yoke without sacrificing the hermeticity of the calorimetry. The end sections of the solenoid are completely hidden behind the endcap calorimeters and a chimney can be arranged to have nearly no interference with the barrel calorimeter.

Our first choice for the barrel calorimetry is Pb/SciFi calorimetry technique and detailed cost estimates are given. Of course, in the barrel section of zero magnetic field any calorimeter techniques can be used. On the other hand, in the endcap sections we need considerable R&D work before choosing the best calorimetry technique.

We propose a simple central muon system in which momentum measurements of muons are made solely by the central tracking device. Precision measurement will not be made by a magnetized iron toroid system. It is shown that a CDF-type muon trigger is made feasible by the solenoid and return yoke and also by the magnetized iron absorber of 1 m in thickness. It is not clear whether it is worth-while to do redundant momentum measurements of muons with a rather massive and costly magnetized-iron toroid system.

Acknowledgement

Cooperation by Hitachi Ltd. for design work of the HCD solenoid is acknowledged.

References

1. F. Abe et al., Nucl. Instr. and Meth. A271(1988)387.
2. G. G. Hanson et al., "Report of the Large Solenoid Detector Group," Experiments, Detectors, and Experimental Areas for the Supercollider (World Scientific, Singapore, 1987), pp. 340-387.
3. See, for example, G. J. Feldman et al.,"$4\pi$ Detectors," Proc. of the 1984 Summer Study on the Design and Utilization of the Superconducting Supercollider, edited by R. Donaldson and J. G. Morfin, Snowmass, CO (1984), p.624; D. Theriot et al., "$4\pi$ Detectors," Proc. of the 1986 Summer Study on the Physics of the Superconducting Supercollider, edited by R. Donaldson and J. Marx, Snowmass, CO (1986), p.351.
4. S. Mori, "Preliminary Studies of Large Solenoids and Related Structure," High Energy Physics in the 1990s, Snowmass, 1988 (World Scientific, Singapore, 1989), pp. 837-840; "Report on Conceptual Design Studies of a Large Superconducting Solenoid (II)," Hitachi Ltd., March 1989 (in Japanese), unpublished.
5. R. Fast et al., "SSC Detector Solenoid," High Energy Physics in the 1990s, Snowmass, 1988 (World Scientific, Singapore, 1989), pp. 841-844; R. Fast et al., Fermilab Internal Report TM-1620[SSC-N-663](September 1989), Fermilab, Batavia, IL, unpublished.
6. For a summary report on large superconducting solenoids built recently see, for example, H. Hirabayashi, "Detector Magnets in High Energy Physics," IEEE Trans. on Magnetics, 24(1988)1256.
7. Design Report for an Indirectly Cooled 3-m Diameter Superconducting Solenoid for the Fermilab Collider Detector Facility (October 1982), Fermilab, Batavia, IL, unpublished; H. Minemura et al., Nucl. Instr. and Meth. A238(1985)18.
8. See, for example, G. G. Haselden, Cryogenic Fundamentals

(Academic Press, London and New York, 1971).

9. R. Wands, J. Grimson, R. Kephart, and D. Theriot, Fermilab Internal Report TM-2750.1113 (May 1982), Fermilab, Batavia, IL, unpublished.
10. H. Hirabayashi et al., Jpn. J. Appl. Phys. 20(1981)2243 and 21(1982)1149.
11. S. Mori and M. Noguchi, Jpn. J. Appl. Phys. 22(1983)812.
12. R. Yamada and M. Wake, Fermilab Internal Report CDF-SDS-11 (March 1982), Fermilab, Batavia, IL, unpublished.
13. R. Yamada, Fermilab Internal Report, CDF-86(January 1981), and TM-1162(January 1983), Fermilab, Batavia, IL, unpublished.
14. We consulted with a honeycomb maker, Yokohama Honeycomb Products. Their facility can handle a single unit volume up to 2.2 m in diameter and about 6 m in length.
15. CDF group, private communication.
16. K. Ogawa et al., Nucl. Instr. and Meth. A238(1985)328.
17. Report of the Task Force on Detector R&D for the Superconducting Super Collider, SSC-SR-1021, SSC Central Design Group, June 1986.
18. R. Diebold et al., CDF Note-106, October 1981, unpublished; L. Nodulman et al., Nucl. Instr. and Meth. 204(1983)351.
19. F. Takasaki et al., Nucl. Instr. and Meth. A262(1987)224 and A260(1987)447; F. Takasaki, "Development of Plastic Scintillation Fibers, Plastic Scintillation Fiber Calorimeter and Its Readout System," High Energy Physics in the 1990s, Snowmass, 1988 (World Scientific, Singapore, 1989), pp. 785-790.
20. P. Jenny et al., "The High Resolution Spaghetti Hadron Calorimeter," NIKHEFH/87-07(1987).
21. R. Wigmans, Nucl. Instr. and Meth. A259(1987)389; R. Wigmans, "Calorimetry at SSC," Experiments, Detectors, and Experimental Areas for the Supercollider (World Scientific, Singapore, 1987), pp. 608-635.
22. The ZEUS Detector, Status Report 1987, ZEUS Collaboration, PRC 87-02, September 1987.
23. R. Wigmans, "The Spaghetti Calorimeter Project at CERN," High Energy Physics in the 1990s, Snowmass, 1988 (World Scientific, Singapore, 1989), pp. 798-805.
24. Y. Asano, private communication.

Figure Captions

Fig. 2-1. Schematic side view of the HCD. All dimensions are in meters.

Fig. 2-2. A quadrant of the end view of the HCD. All dimensions are in meters.

Fig. 2-3. Schematic side view of the central section of the CDF detector.

Fig. 3-1. Schematic drawing of the end section of the CDF solenoid at the chimney side. The side view of an axial support is also shown. An enlarged view shows the coil conductor and FRP layer. All the dimensions are in mm.

Fig. 3-2. Magnetic flux versus critical current for a standard short sample. The load line corresponds to the maximum magnetic field experienced by the conductor.

Fig. 3-3. Parameter $\Gamma$ versus $T_{max}$ for aluminum with RRR = 2450.

Fig. 3-4. (a)Schematic side and end views of the end section of the HCD solenoid and (b)schematic drawing of a module end with a flange for module connection. A fixture to provide the axial preload to the coil is also shown in (b).

Fig. 3-5. (a)Assembly procedure of a honeycomb outer vacuum wall shown from the end view. An aluminum block with an inner plate, a honeycomb core piece andan outer plate are assembled and processed to form a quadrant section of a vacuum wall cylinder. Four quadrant sections are welded. (b)Side view of the honeycomb vacuum wall.

Fig. 3-6. Schematic diagram of the arrangement of the radial and axial support system of the CDF solenoid.

Fig. 3-7. Schematic section view of the radial support. All dimensions are in mm. Although not shown explicitly, a liquid helium intercept is located at the support anchor.

Fig. 3-8. Effective material thickness of the HCD solenoid as a function of the axial distance from the interaction point. Honeycomb vacuum walls are installed at the axial distance from 4 to 6 m.

Fig. 4-1. Monte Carlo simulations of energy losses of electrons in aluminum absorbers.

Fig. 4-2. Monte Carlo simulations of RMS energy losses of electrons in aluminum absorbers as a function of the electron energy.

Fig. 4-3. Monte Carlo simulations of RMS energy losses of electrons as a function of the thickness of an aluminum absorber.

Fig. 4-4. Measured energy resolutions for electrons as a function of the thickness of an absorber which was placed in front of a calorimeter [15].

Fig. 4-5. Measured energy resolution of an SF03 lead glass counter (18 $X_0$) with aluminum absorbers of different thickness in front [16].

Fig. 5-1.(a)Solenoid and the barrel and endcap calorimeters. (b)Simplified model to simulate the arrangement of the endcap calorimeter, the solenoid, and the barrel calorimeter seen from a particle produced at the interaction region in the direction around y = 1.6. In most of the simulations the calorimeters are replaced by "lead" absorbers with the density of 4/5 of normal lead.

Fig. 5-2. Average energy deposition distributions calculated in the coil and the endcap and barrel calorimeters for 20 GeV electrons. The electrons are incident parallel to the edge and distributed uniformly in the x direction. The calorimeters are substituted by normal lead absorbers.

Fig. 5-3. Average energy deposition distributions for 20 GeV electrons incident parallel to the edge of the endcap calorimeter. (a)The frame of the endcap calorimeter is made of an aluminum plate of 2 cm in thickness and (b) of an iron plate of 1 cm in thickness.

Fig. 5-4. Energy dependence of fractional energy depositions as a function of the incident electron energy. The frame of the endcap calorimeter is a 2-cm aluminum plate. The incident electrons are incident parallel to the edge at x = 1 cm.

Fig. 5-5. Average energy deposition distributions for 20 GeV electrons. The frame of the endcap calorimeter is a 2-cm aluminum plate. The incident angles of the electrons with respect to the frame edge are (a) $0^\circ$, (b) $5^\circ$, (c) $3^\circ$, and (d) $-3^\circ$.

Fig. 5-6. Average energy deposition distributions for 20 GeV electrons. The frame of the end cap calorimeter is a 1-cm iron plate. The incident angles of the electrons with

respect to the frame edge are (a) 0° and (b) 5°.

Fig. 6-1. End view of the barrel calorimeter with transverse segmentation of $\Delta\eta = 0.04$ and $\Delta\phi = 0.04$.

Fig. 6-2. Schematic drawing of the EM section of a barrel calorimeter module which has two longitudinal segmentations. In the upstream and downstream sections 1-mm fibers are embedded in the horizontal and vertical directions, respectively. The figure shows a case of 2 x 2 finer segmentation in readout. Two light outputs corresponding to fibers in a section, $XL_1$ and $XR_1$ for example, form a subsection in the readout system.

Fig. 6-3. Energy resolution for electron and hadron detection with a compensating lead/plastic-scintillator calorimeter as a function of the thickness of the readout layers [23].

Fig. 7-1. (a)Deflection angle versus radius for a 50 GeV muon at 90 degrees. (b)Schematic drawing of the muon trigger system.

Table II. Main Parameters of the HCD solenoid

| Items | Parameters |
|---|---|
| Vacuum vessel | |
| Diameter: inner/outer | 4500 mm/5300 mm |
| Length | 15000 mm |
| Material | A5083 Aluminum |
| Wall thickness | |
| Normal: inner/outer | 7 mm/40 mm |
| Honeycomb: outer | 75 mm |
| Solenoid | |
| Central field | 1.7 Tesla |
| Stored energy | 300 MJ |
| Current(13600 A/cm) | 8000 A |
| Inductance | 9.4 H |
| Winding scheme | Single layer helix |
| Conductor | |
| Composition | Al stabilized NbTi |
| Dimension | 5.68 x 28 $mm^2$ |
| $J_0$ | 51.6 $A/mm^2$ |
| $E_0 J_0^2$ | $8.0 \times 10^{23}$ $JA^2/m^4$ |
| Outer support cylinder | |
| Material | 2219-T851 Aluminum |
| Thickness | 14 mm |
| Overall material thickness | 1.18 $X_0$ /0.86 $X_0$ * |
| Cold mass | 24 t |
| Total weight | 74 t |
| Liquid helium cryogenics | Forced flow two-phase |

*The second value corresponds to the sections where the outer vacuum walls have honeycomb walls.

Table III. General comparison of module arrangements

| Items | | | Number of modules | | |
|---|---|---|---|---|---|
| | | | 1 | 2 | 4 |
| Module length (m) | | | 15 | 7.5 | 3.75 |
| Design | a.Protectio | | C | B | A |
| | b.Strength | | C | B | A |
| | c.Space utilization & connection | | A | B | C |
| Fabrication & testing | a.Precision: | Manufacturing | B | B | A |
| | | Machining | D | D | A |
| | b.Winding : | Mandrel | A | A | A |
| | | Shrink fit | D | B | A |
| | c.Inner winding | | A | A | A |
| | d.Assembly | | D | A | A |
| | e. Testing | | B | B | B/A |
| Schedule | | | A | A | A |
| Transportation | | | A | A | A |
| Repair work | | | C | C/B | B |

Classification

A: Relatively easy

B: Rather difficult

C: Difficult

D: Very difficult; new facilities required

Table IV. Conductor parameters

| Items | Design values |
|---|---|
| Superconductor cross section and dimensions (mm) | 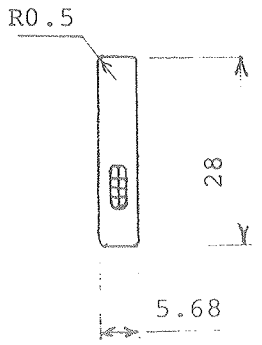  |
| Dimension | 5.68 x 28 $mm^2$ |
| Superconductor materials | Nb-46.5 wt% Ti |
| Number of stranded conductors | 8 - 10 |
| Base conductor | |
| Diameter | 1.4 mm |
| Filament diameter | 23 μm |
| Number of filaments | 1850 |
| RRR of copper stabilizer | 216 |
| Aluminum stabilizer | |
| RRR | ≅ 2500 |
| Area | 144 $mm^2$ |
| NbTi/Cu/Al ratio | 1/1/20 |
| Standard short sample current at 4.2 K | 16 kA at 2 Tesla<br>11 kA at 4 Tesla |
| Unit length | 5.5 - 8 km |

Table V. Material thicknesses of various components of the HCD solenoid.

| Component | Material | Length (mm) | Radiation length |
|---|---|---|---|
| Inner vac. cyl. | Al | 7 | 0.079 |
| Inner rad. shld | Al | 2 | 0.022 |
| Conductor | Al/NbTi/Cu | 28 | 0.433 |
| Coil insulation | FRP etc. | 3 | 0.018 |
| Support cyl. | Al | 14 | 0.157 |
| Outer rad. shld | Al | 2 | 0.022 |
| Outer vac. cyl. | Al | 40/75* | 0.449/0.131* |
| Total | | | 1.180/0.862* |

*The second values correspond to the honeycomb arrangement.

Table VI. Main parameters of the barrel calorimeter.

| | | |
|---|---|---|
| General characteristics | | |
| Composition | Pb:SciFi = 4:1 (in volume) | |
| Geometry | Semi-tower | |
| Number of tower modules | 13440 | |
| Rapidity coverage | $\pm$ 1.6 | |
| Weight (t) | 5760 (690: EM, 5070:hadron) | |
| Total number of PM tubes | 67200 | |
| EM calorimeter | | |
| Depth | 30 $X_0$ ($\cong$ 25 cm) | |
| Fiber diameter | 1 mm | |
| Fiber arrangement | Transverse | |
| Optical arrangement | WLS-LG(plate + fibers)-PM | |
| Number of longitud. segmentations | 2 | |
| Trans. segmentation ($\Delta\eta$ x $\Delta\phi$) | | |
| Depth ($X_0$) | Tower | Readout |
| 0 - 10 | 0.04 x 0.04 | 0.02 x 0.04 |
| 10 - 30 | 0.04 x 0.04 | 0.04 x 0.02 |
| Number of towers | 13440 | |
| Number of PM tubes | 53760 | |
| Hadron calorimeter | | |
| Depth including EM calorimeter | 10 absorption lengths | |
| Fiber diameter | 2 mm | |
| Number of longitud. segmantation | 1 | |
| Trans. segmentation ($\Delta\eta$ x $\Delta\phi$) | 0.04 x 0.04 | |
| Number of towers | 13440 | |
| Number of PM tubes | 13440 | |

Table VII. Cost estimates of barrel calorimeters.

Scintillating fibers

| Items | Diameter (mm) | Weight (t) | Length ($10^7$ m) | Unit cost* (yen) | Cost ($10^8$ yen) |
|---|---|---|---|---|---|
| EM | 1 | 15.7 | 1.94 | 50 x 2/3 | 6.5 |
| Hadron | 2 | 115.2 | 3.54 | 100 x 2/3 | 23.7 |
| Total | | 131 | | | 30 |

*Cost reduction due to large quantity was assumed to be 2/3. The unit cost of plate scintillators is about $6.5 \times 10^6$ yen/ton which corresponds to about $8.5 \times 10^8$ yen for the total weight 131 tons.

WLS, Light guide ($2 \times 10^8$ yen
(2000 yen/channel)

Photomultiplier tubes and power supplies etc.

| Items | Number of PM tubes | Unit cost (yen) | Cost ($10^8$ yen) |
|---|---|---|---|
| EM | 53760 | 30000 | 16.1 |
| Hadron | 13440 | 30000 | 4.0 |
| Total | 67200 | | 20 |

Lead

| | |
|---|---|
| Special process lead | 300 yen/kg |
| Total weight | 5760 t |
| Total lead cost | $17 \times 10^8$ yen |

Overall material cost
without readout electronics $69 \times 10^8$ yen

## VIII. Cost comparison of Pb/SciFi barrel calorimeter

A. Transverse segmentation ( $\Delta\eta \times \Delta\phi$ )

| Items | Depth ($X_0$) | Tower | Readout | Number of PM tubes | Cost* ($10^8$ yen) |
|---|---|---|---|---|---|
| EM | 0 – 10 | 0.03x0.03 | 0.015x0.03 | 46592 | 14.0 |
| | 10 – 30 | 0.03x0.03 | 0.03x0.015 | 46592 | 14.0 |
| Hadron | | 0.03x0.03 | 0.03x0.03 | 23296 | 7.0 |
| Total | | | | 116480 | 35 |

*Unit cost = 30000 yen

B. Fiber diameter of hadron calorimeters

Unit cost: 50 x 2/3 yen/m for 1 mm fiber
75 1.5 mm
100 2 mm

Weight of SciFi : 115.2 t

| Diameter (mm) | Length ($10^7$ m) | Cost (had) ($10^8$ yen) | Cost(had+EM) ($10^8$ yen) |
|---|---|---|---|
| 1 | 14.2 | 47.5 | 54.0 |
| 1.5 | 6.33 | 31.7 | 38.2 |
| 2 | 3.56 | 23.7 | 30.2 |

C. Overall material cost table (in units of $10^8$ yen)

| Transverse segmentation ($\Delta\eta$ x $\Delta\phi$) | Hadron calorimeter fiber diameter (mm) | | |
|---|---|---|---|
| | 1 | 1.5 | 2 |
| 0.03 x 0.03 | 109 | 93 | 85 |
| 0.04 x 0.04 | 93 | 77 | 69 |

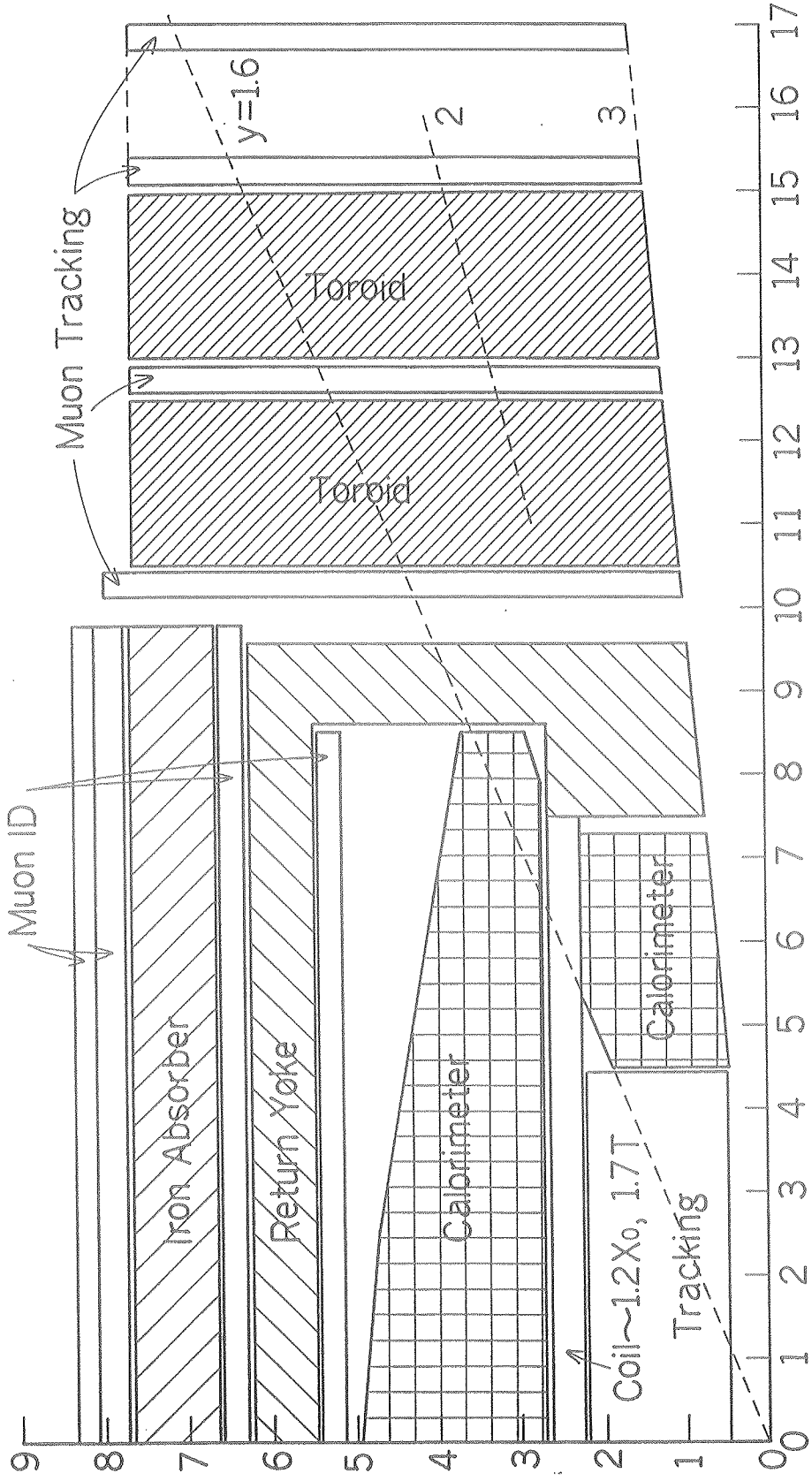
Muon Tracking
y=1.6
2
3
Toroid
Toroid
Muon ID
Iron Absorber
Return Yoke
Calorimeter
Calorimeter
Coil~1.2X₀, 1.7T
Tracking
0
1
2
3
4
5
6
7
8
9
10
11
12
13
14
15
16
17

Figure 2-1.

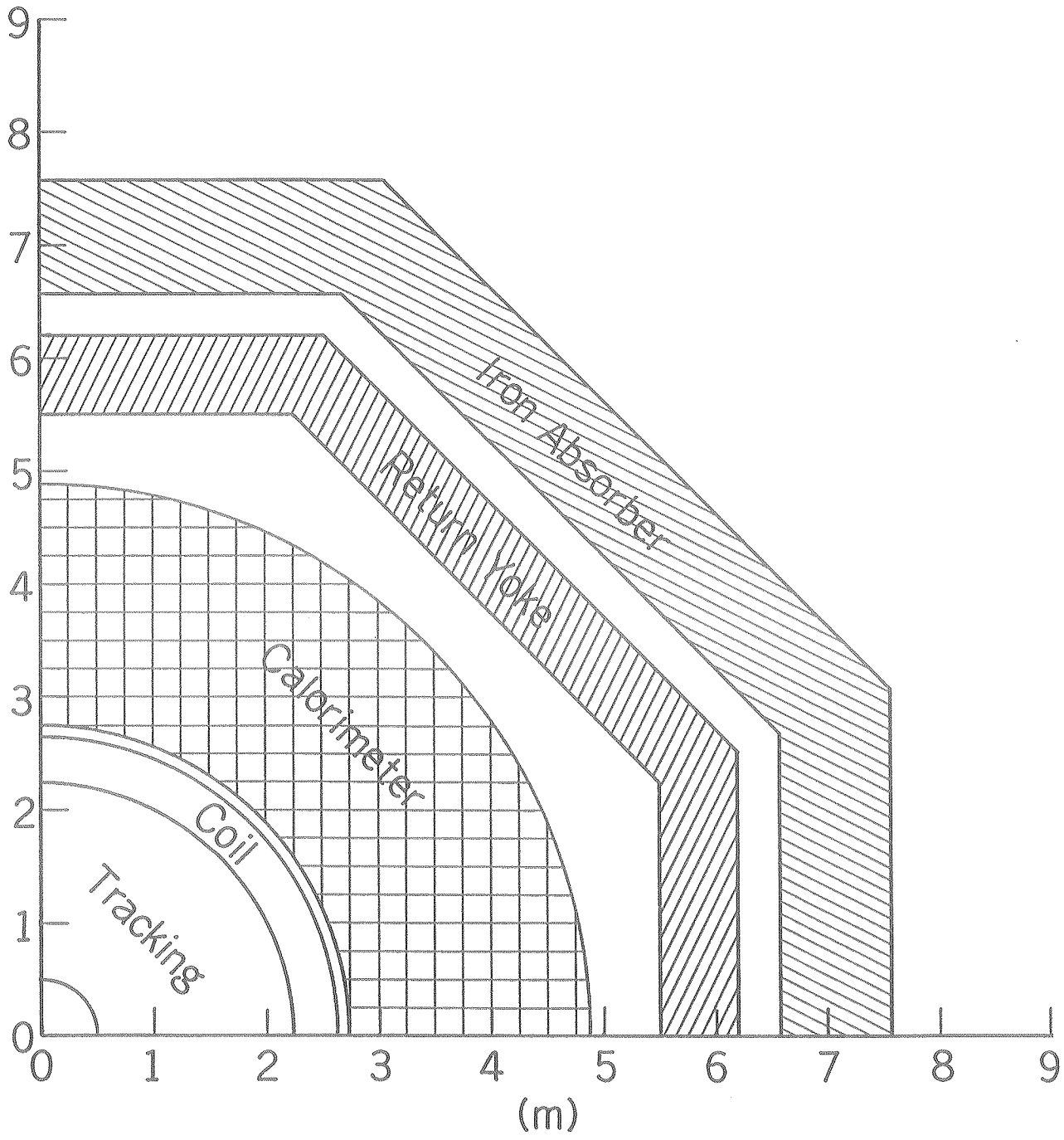
Iron Absorber
Return Yoke
Calorimeter
Coil
Tracking
0
1
2
3
4
5
6
7
8
9
(m)

Figure 2-2.

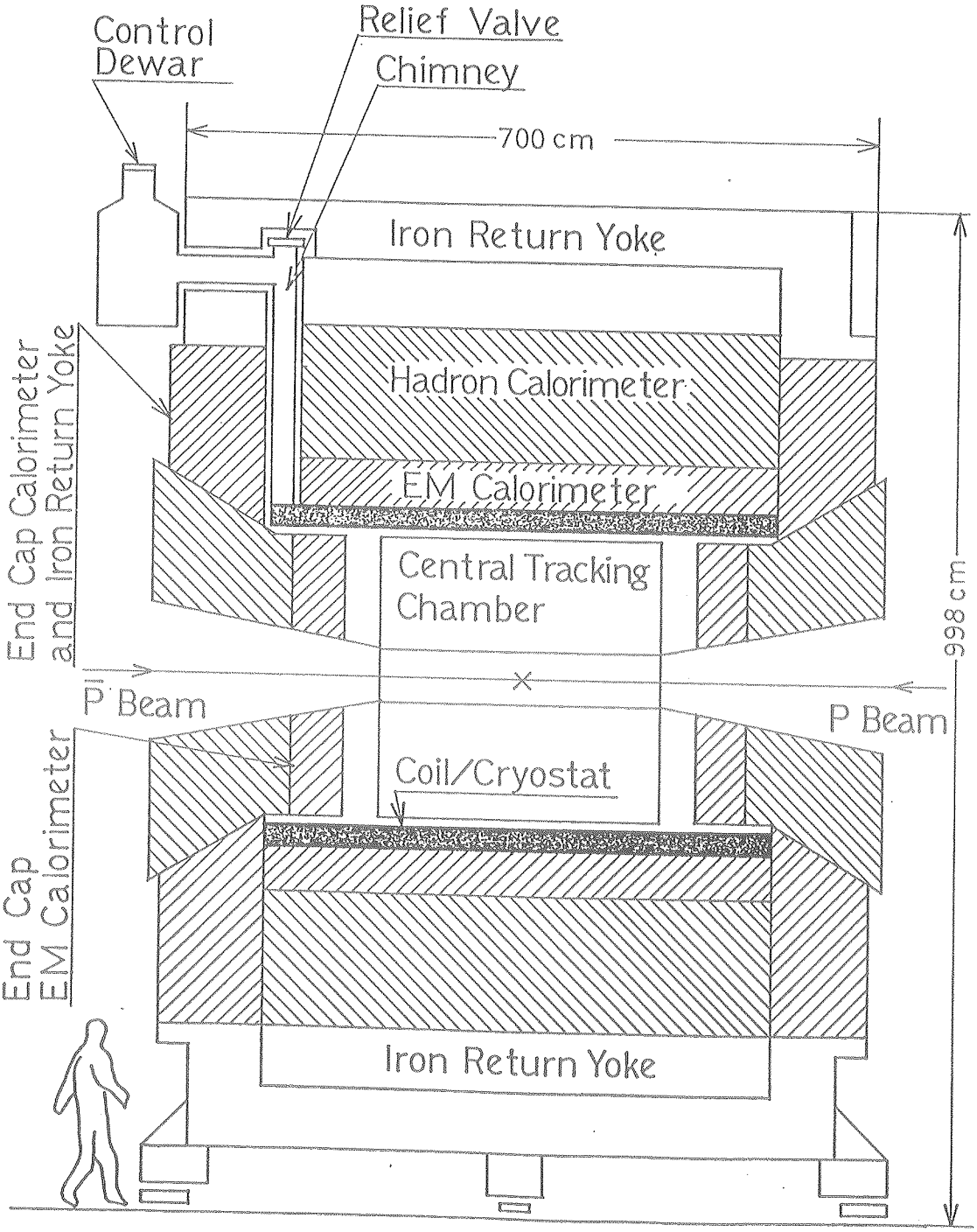
Control Dewar
Relief Valve
Chimney
700 cm
Iron Return Yoke
End Cap Calorimeter and Iron Return Yoke
Hadron Calorimeter
EM Calorimeter
Central Tracking Chamber
998 cm
P Beam
P Beam
Coil/Cryostat
End Cap EM Calorimeter
Iron Return Yoke

Figure 2-3.

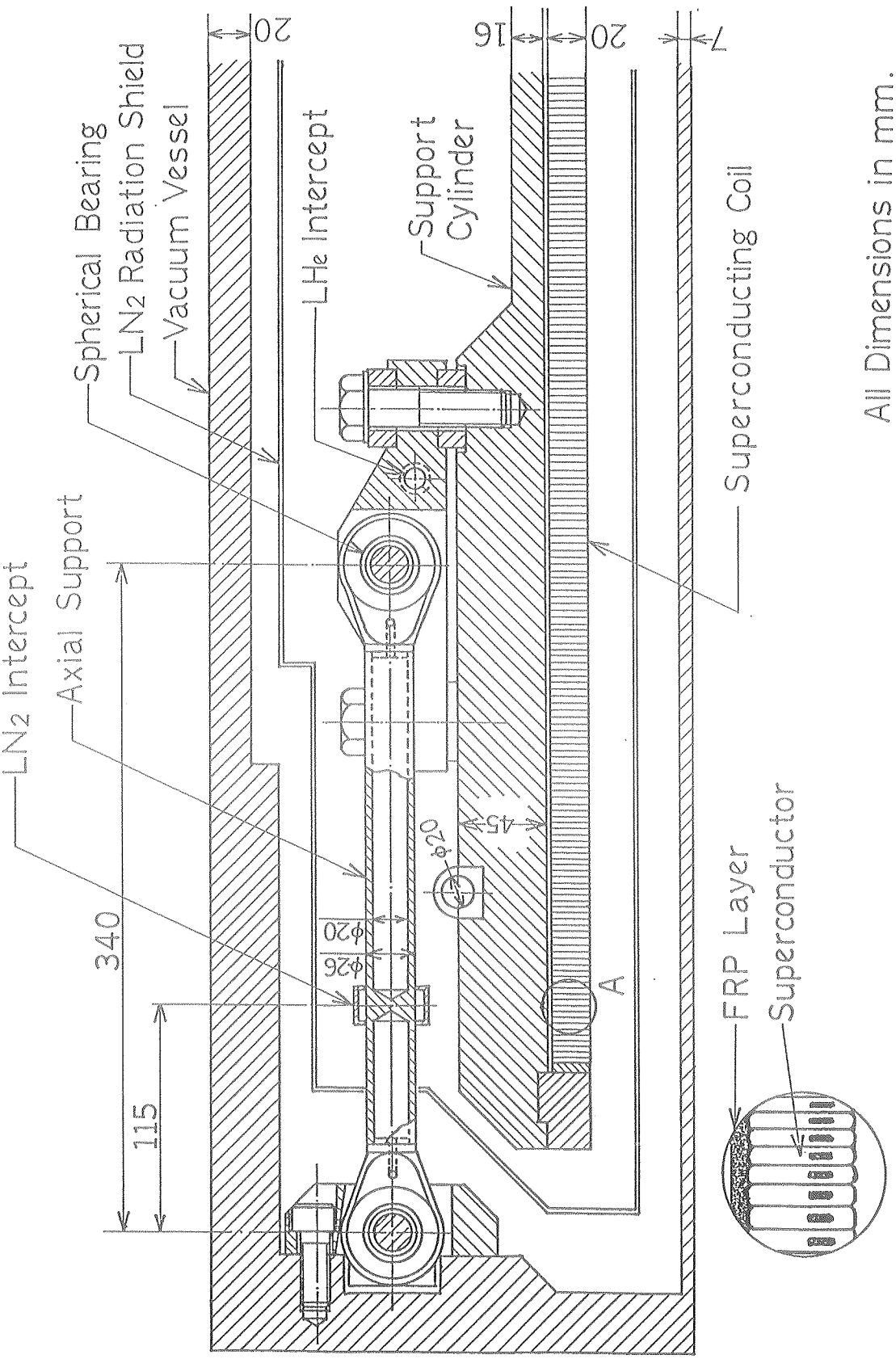
Spherical Bearing
LN2 Radiation Shield
Vacuum Vessel
LHe Intercept
Support Cylinder
Superconducting Coil
LN2 Intercept
Axial Support
340
115
φ20
φ26
φ20
45
20
16
20
7
A
FRP Layer
Superconductor
A
All Dimensions in mm.

Figure 3-1.

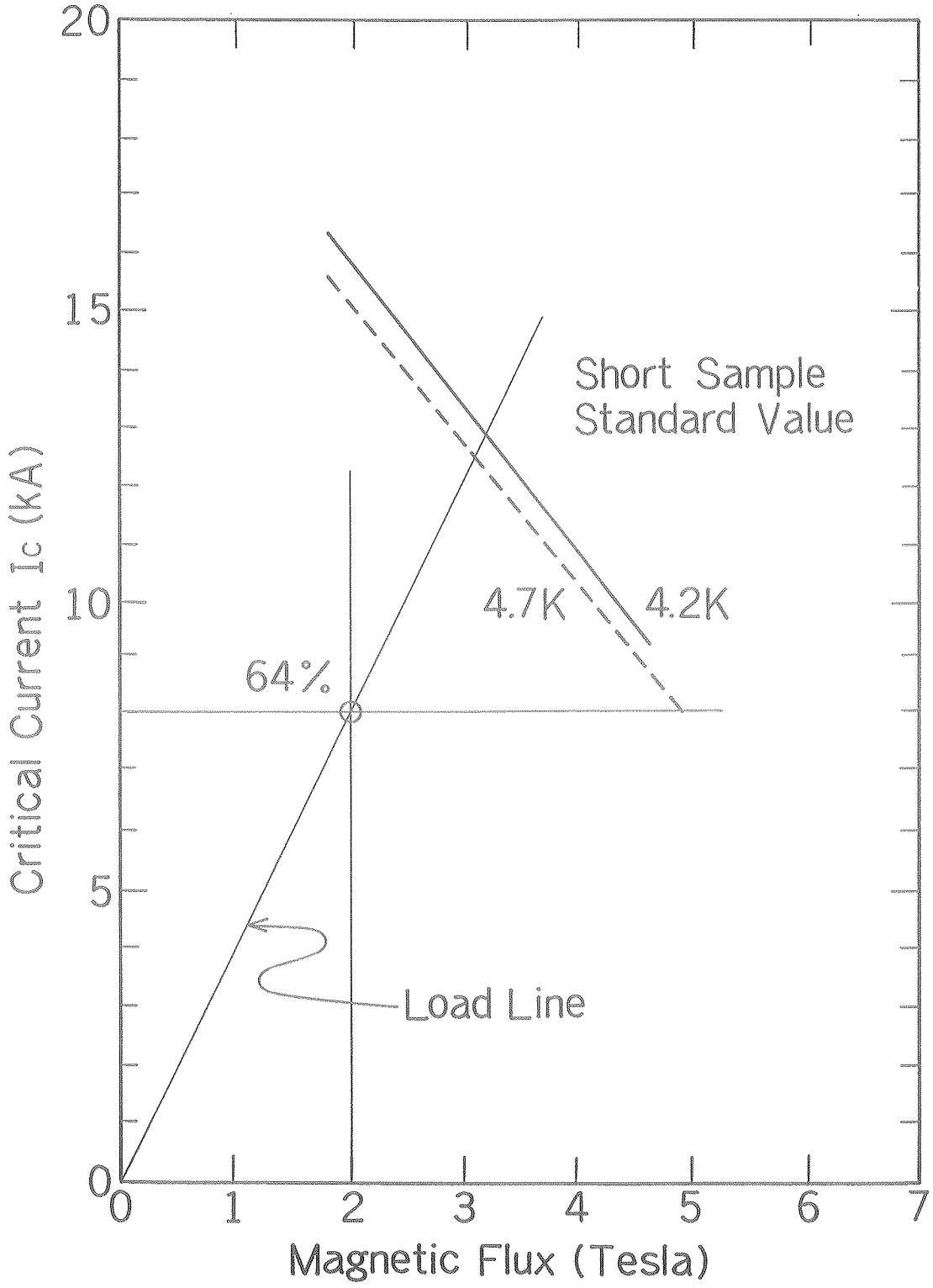
20
15
10
5
0
0
1
2
3
4
5
6
7
Critical Current Ic (kA)
Magnetic Flux (Tesla)
Short Sample
Standard Value
4.7K
4.2K
64%
Load Line

Figure 3-2.

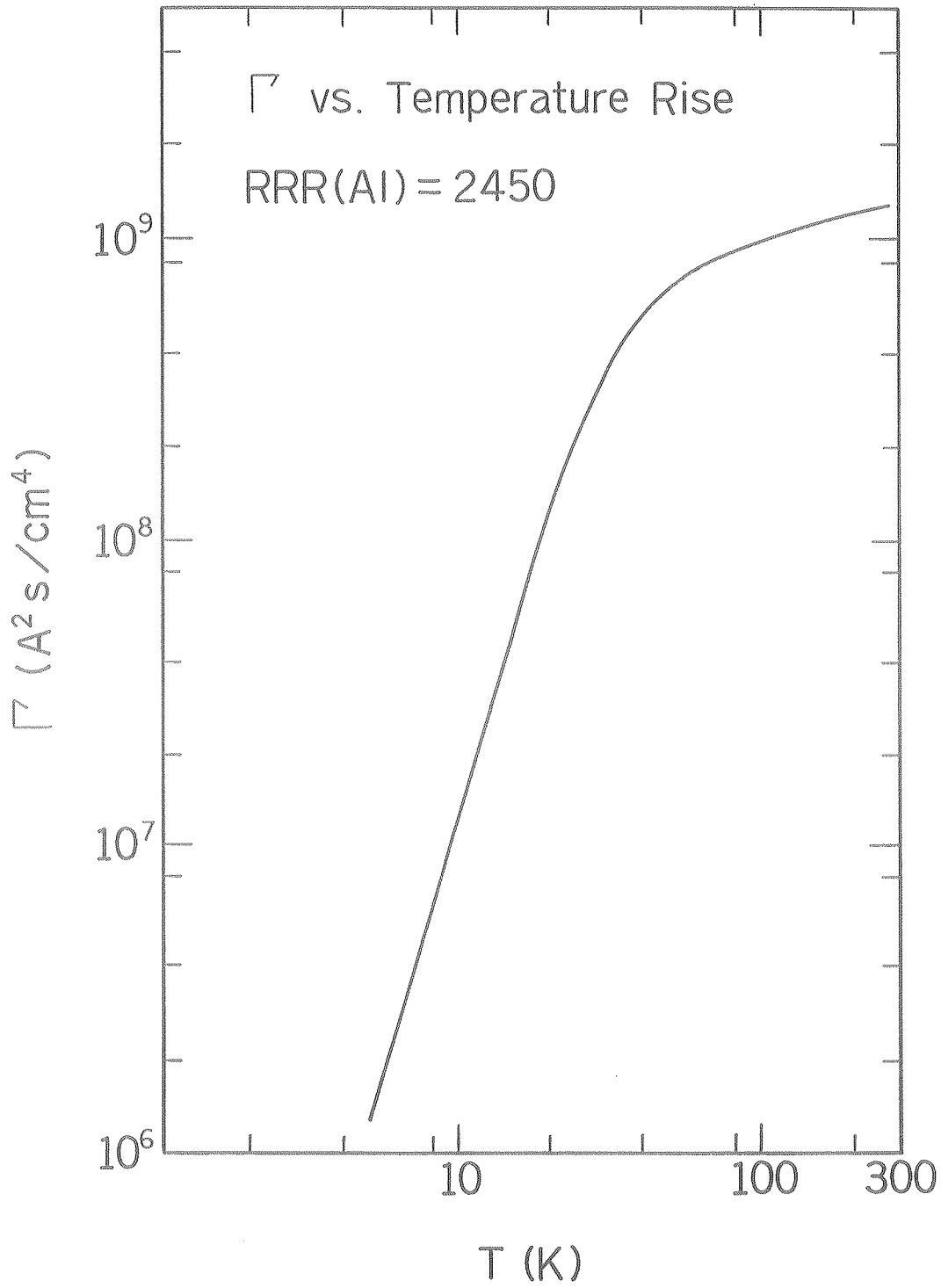
Γ′ vs. Temperature Rise
RRR(Al) = 2450
Γ′ (A²s/cm⁴)
10⁹
10⁸
10⁷
10⁶
10
100
300
T (K)

Figure 3-3.

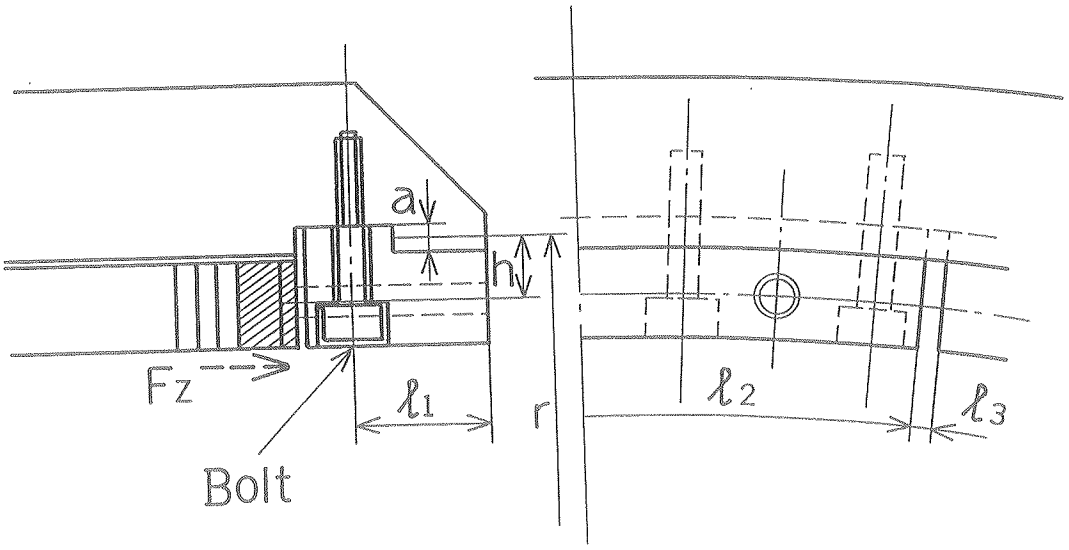
a
h
Fz
ℓ1
r
ℓ2
ℓ3
Bolt

(a)

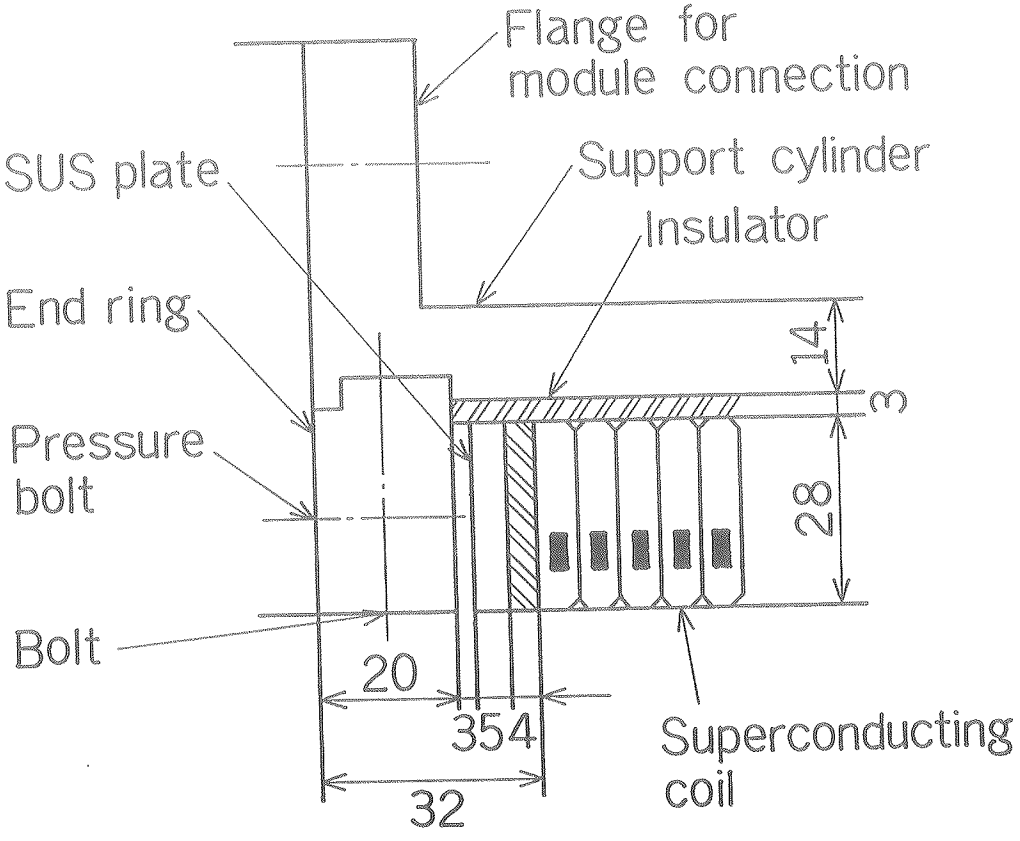
Flange for
module connection
SUS plate
Support cylinder
Insulator
End ring
14
3
Pressure
bolt
28
Bolt
20
354
32
Superconducting
coil

(b)

Figure 3-4.

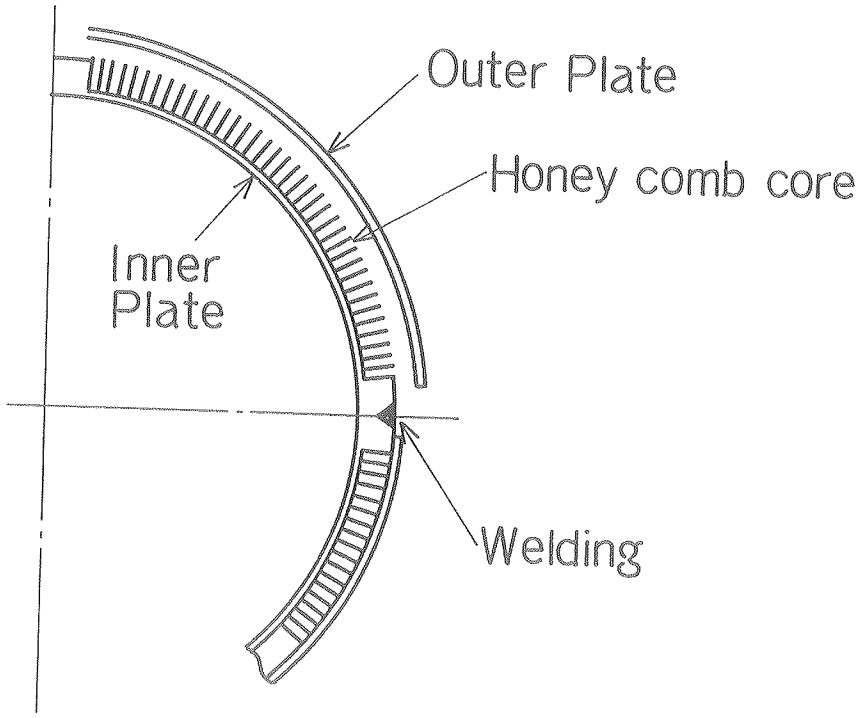
Outer Plate
Honey comb core
Inner Plate
Welding

(a)

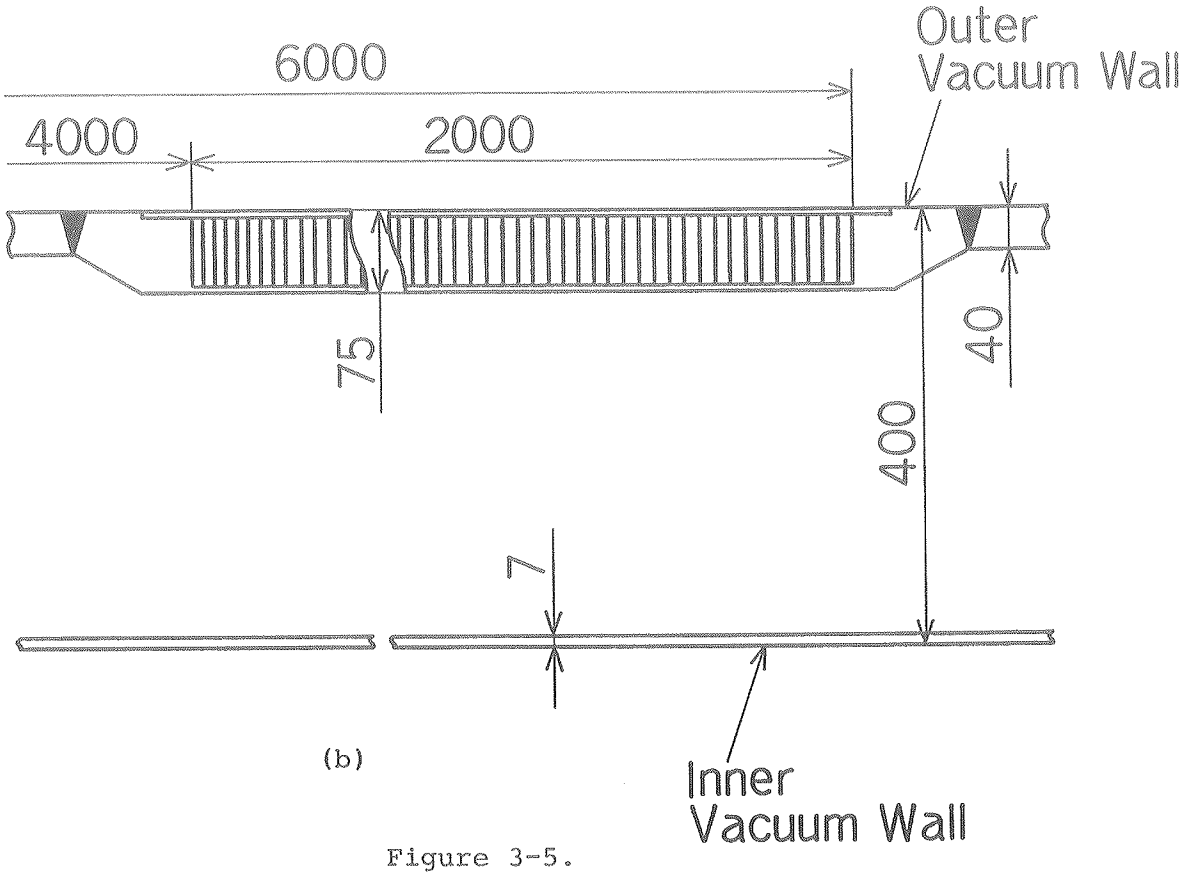
6000
4000
2000
Outer Vacuum Wall
75
40
400
7
Inner Vacuum Wall

(b)

Figure 3-5.

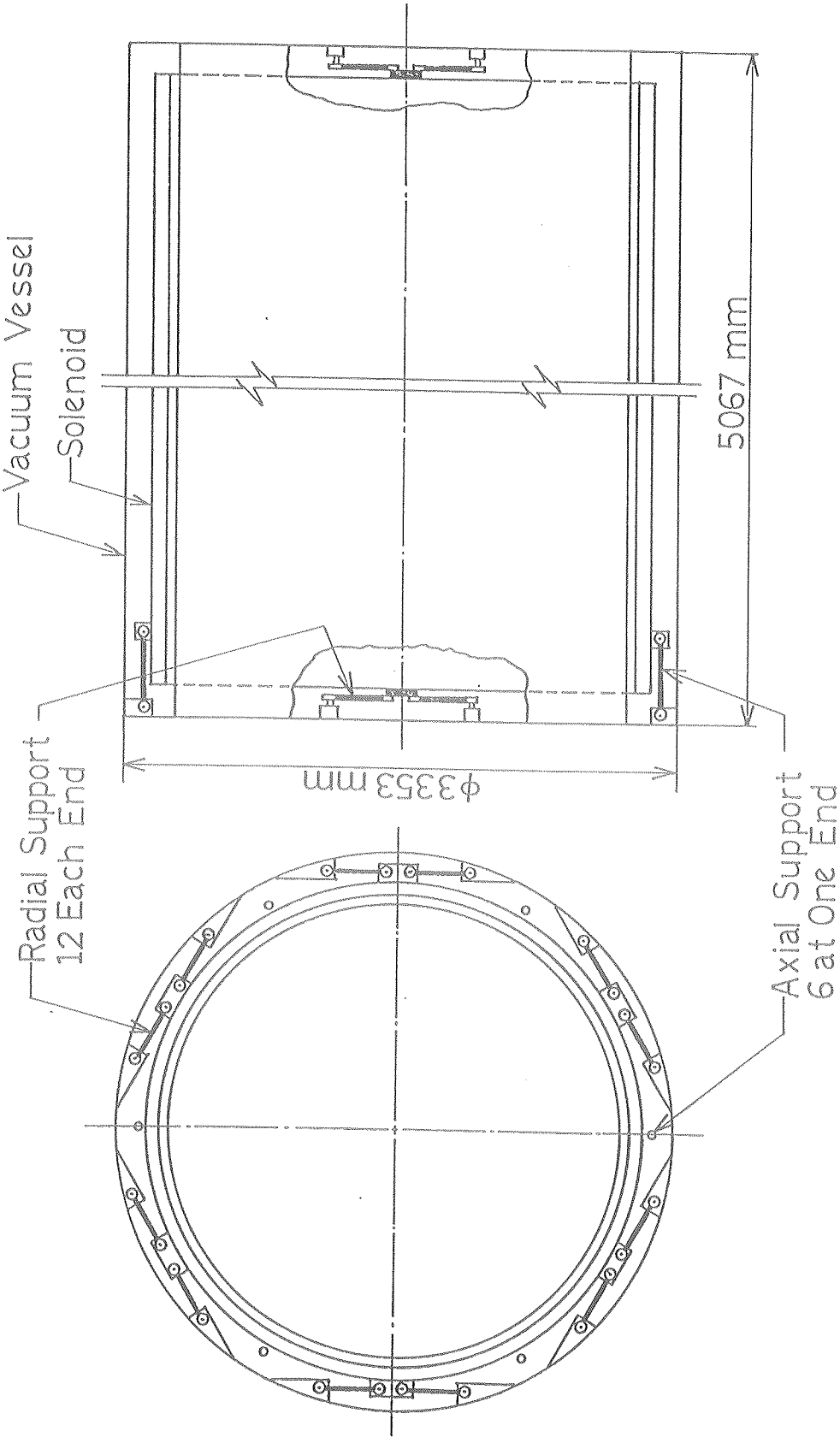
Vacuum Vessel
Solenoid
5067 mm
φ3353 mm
Radial Support
12 Each End
Axial Support
6 at One End

Figure 3-6.

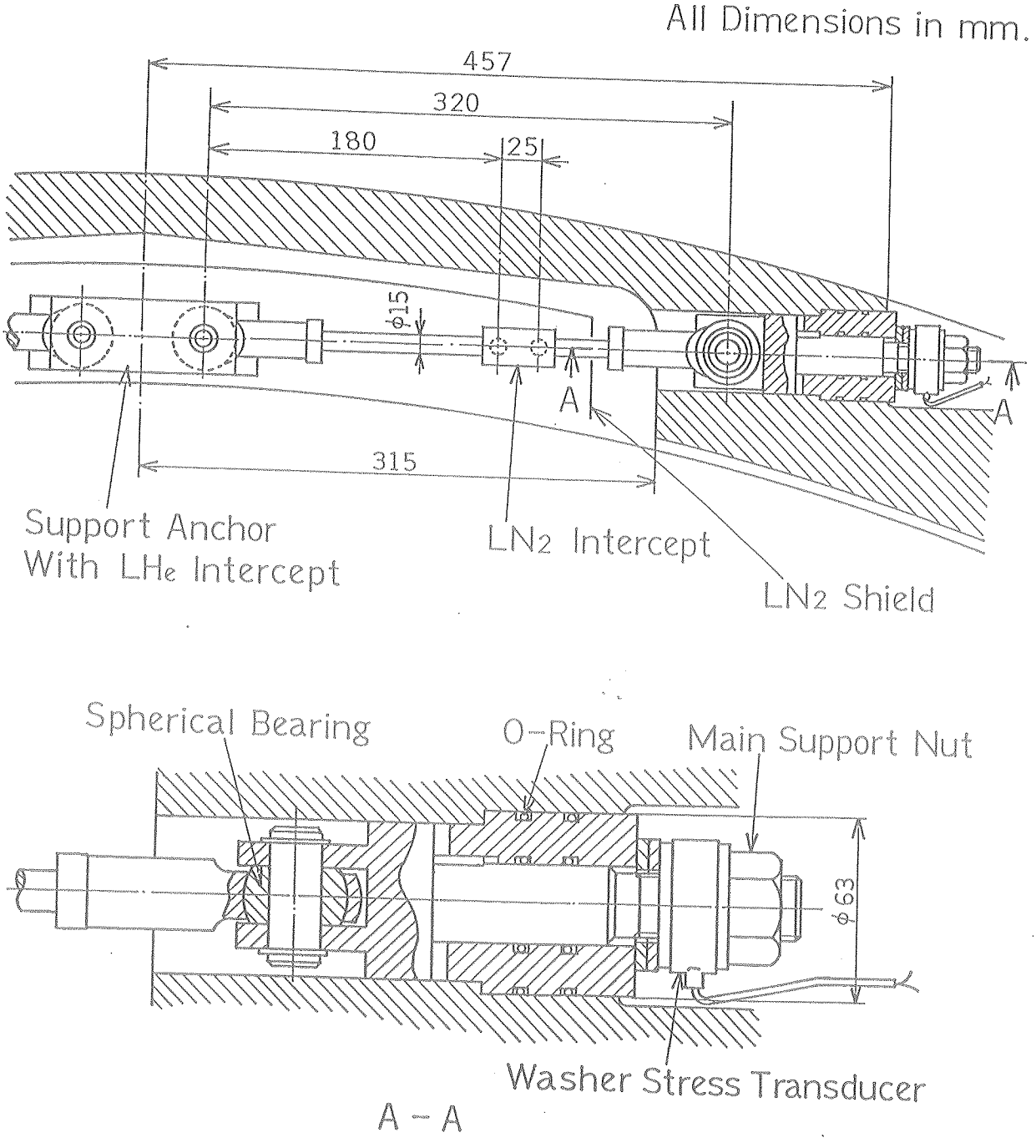
All Dimensions in mm.
457
320
180
25
ϕ15
A
A
315
Support Anchor
With LHe Intercept
LN2 Intercept
LN2 Shield
Spherical Bearing
O-Ring
Main Support Nut
ϕ63
Washer Stress Transducer
A - A

Figure 3-7.

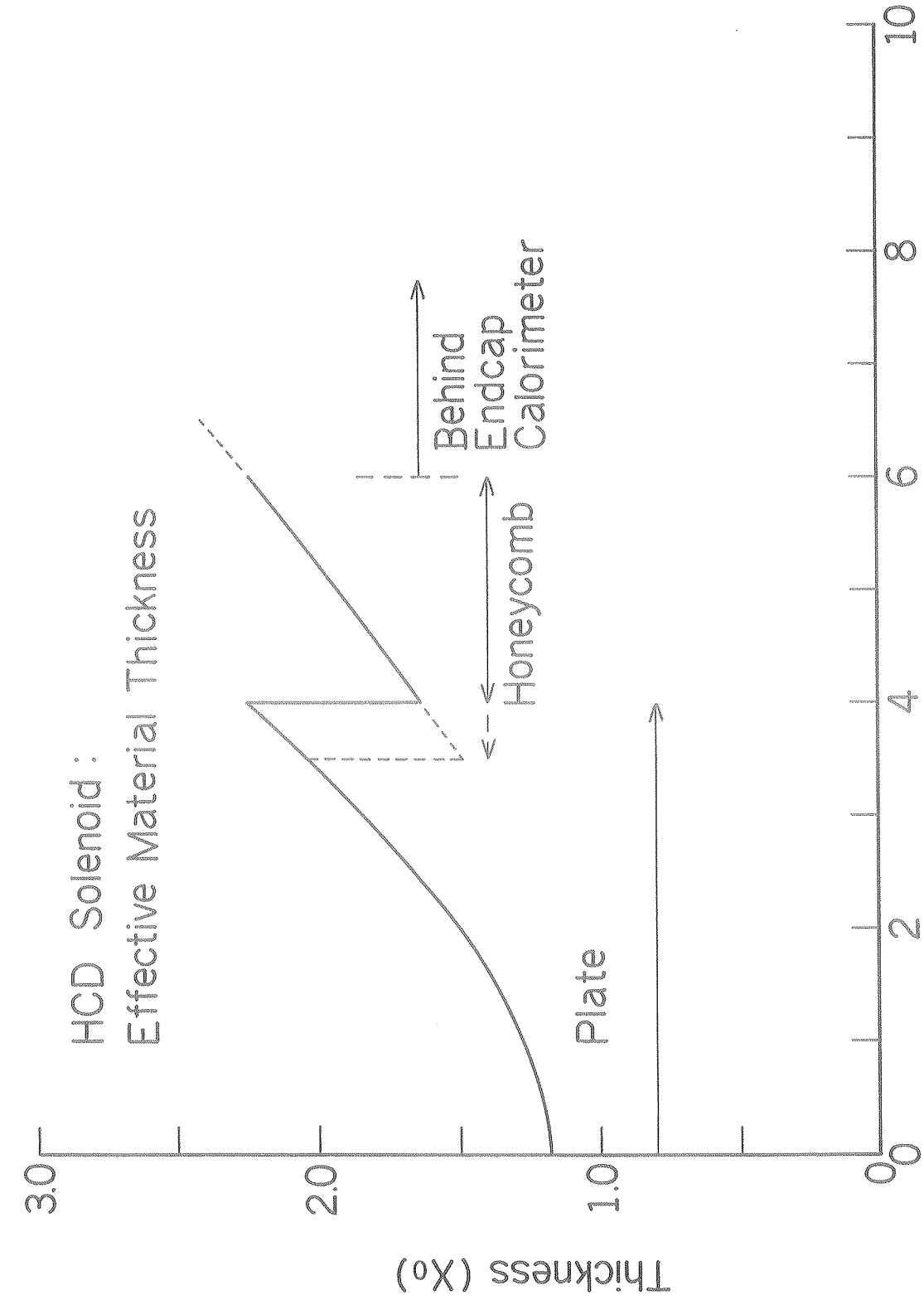
HCD Solenoid :
Effective Material Thickness
Behind Endcap Calorimeter
Honeycomb
Plate
Thickness ($X_0$)
Axial Distance (m)
0
2
4
6
8
10
1.0
2.0
3.0

Figure 4-8.

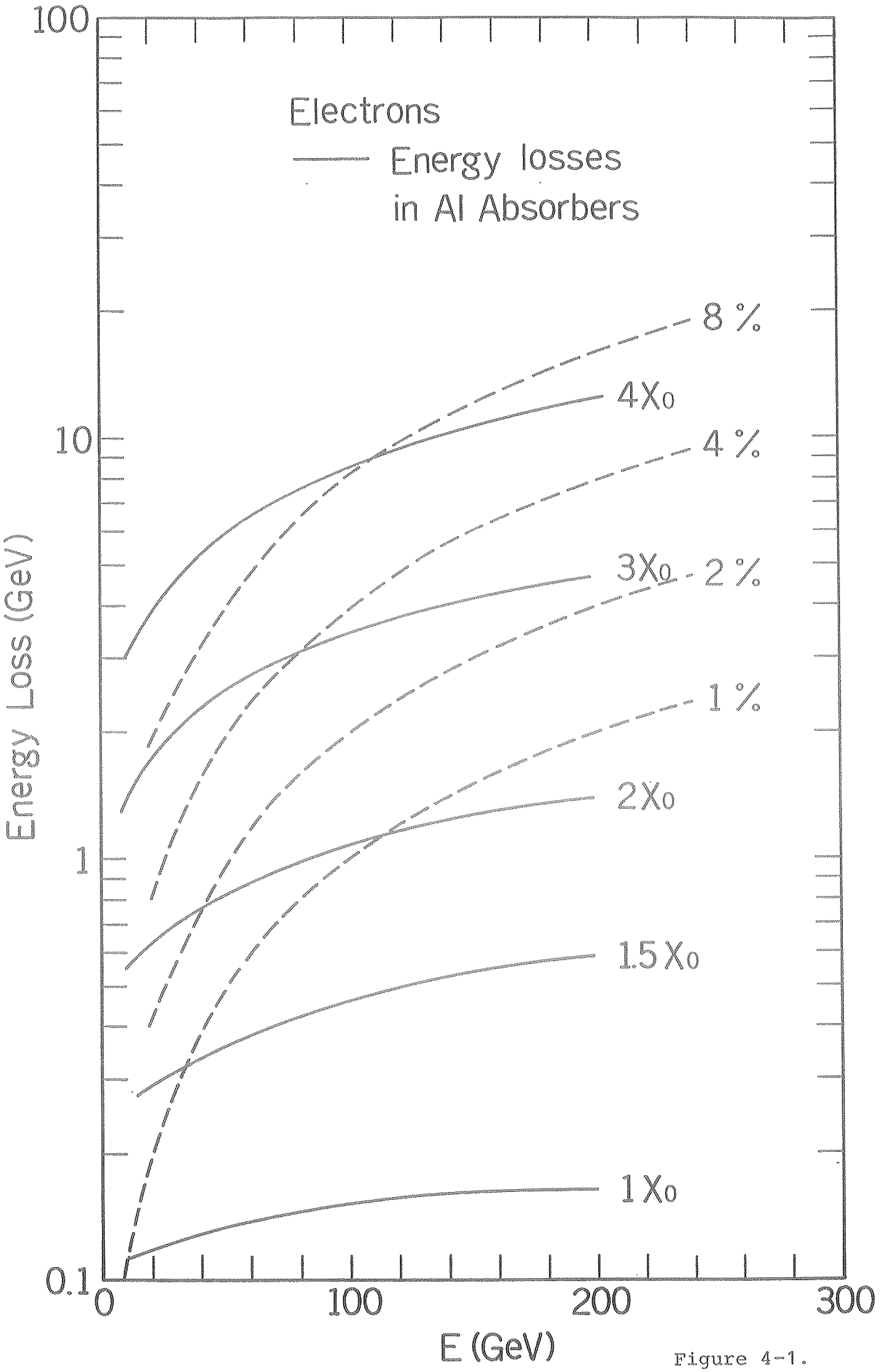
Electrons
Energy losses
in Al Absorbers
8 %
4X0
4 %
3X0
2 %
1 %
2X0
1.5X0
1X0
Energy Loss (GeV)
100
10
1
0.1
0
100
200
300
E (GeV)

Figure 4-1.

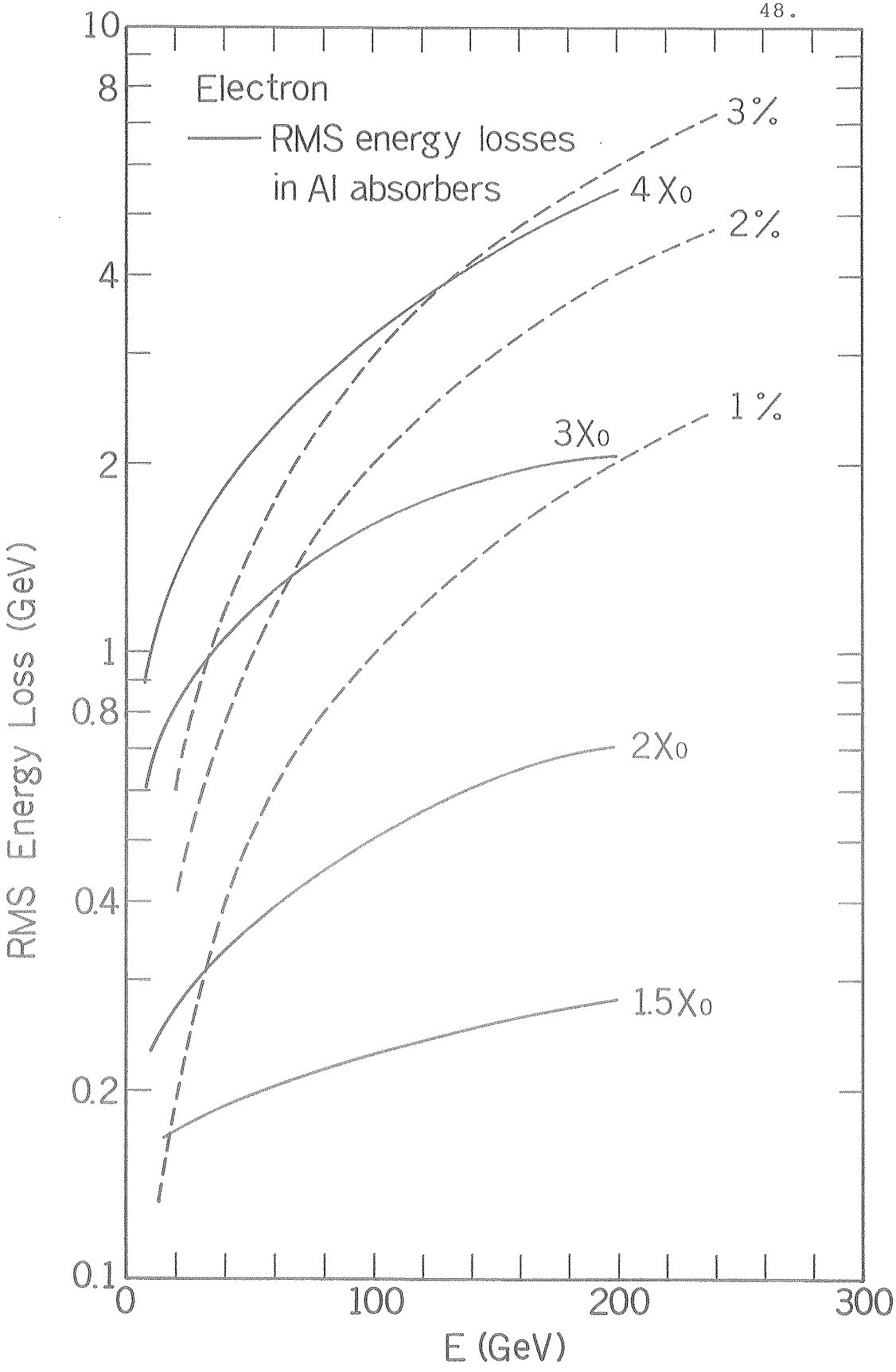
Electron
RMS energy losses
in Al absorbers
3%
4 X0
2%
1%
3X0
2X0
1.5X0
RMS Energy Loss (GeV)
E (GeV)
10
8
4
2
1
0.8
0.4
0.2
0.1
0
100
200
300

Figure 4-2.

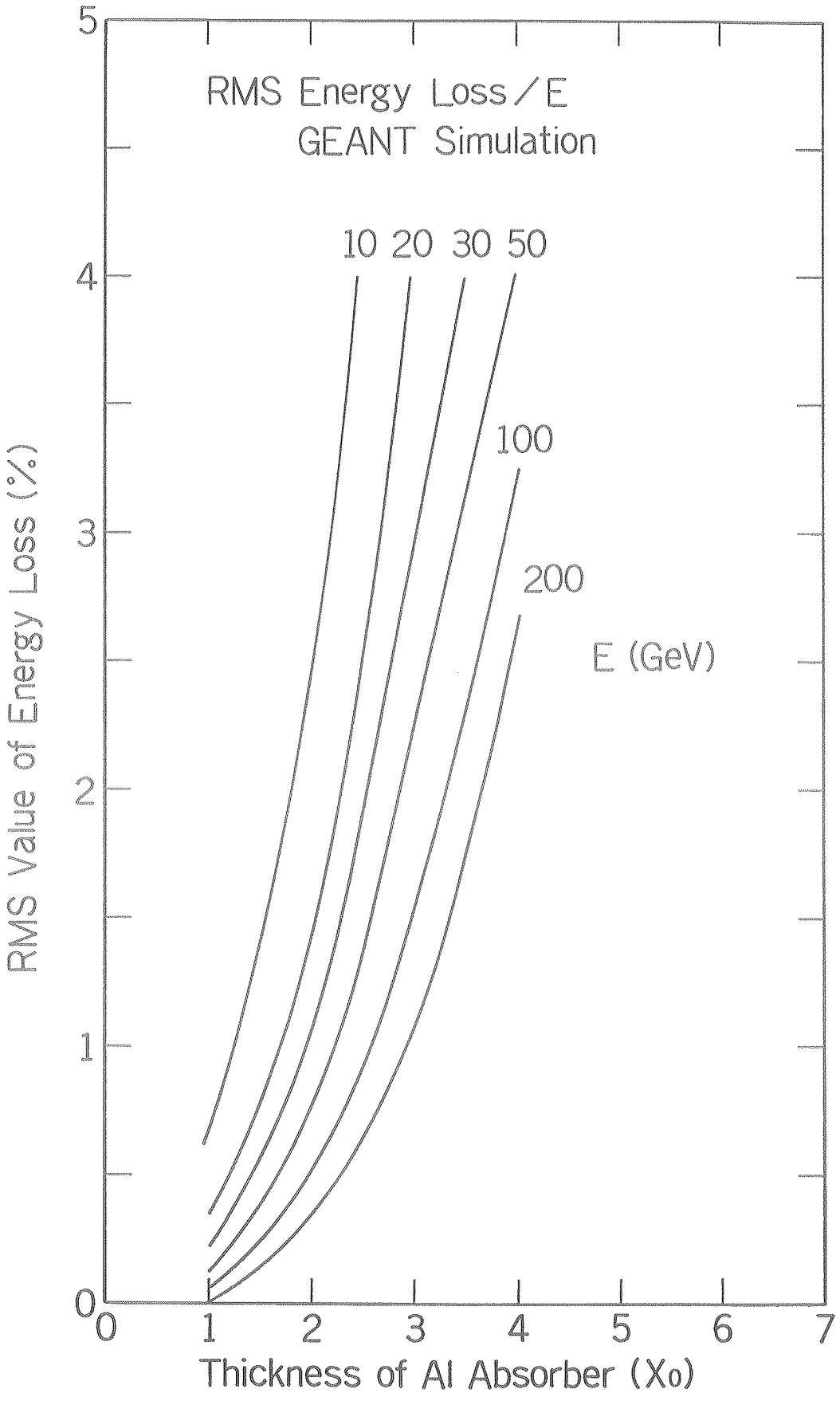
RMS Energy Loss / E
GEANT Simulation
10 20 30 50
100
200
E (GeV)
RMS Value of Energy Loss (%)
Thickness of Al Absorber (Xo)
0
1
2
3
4
5
6
7

Figure 4-3.

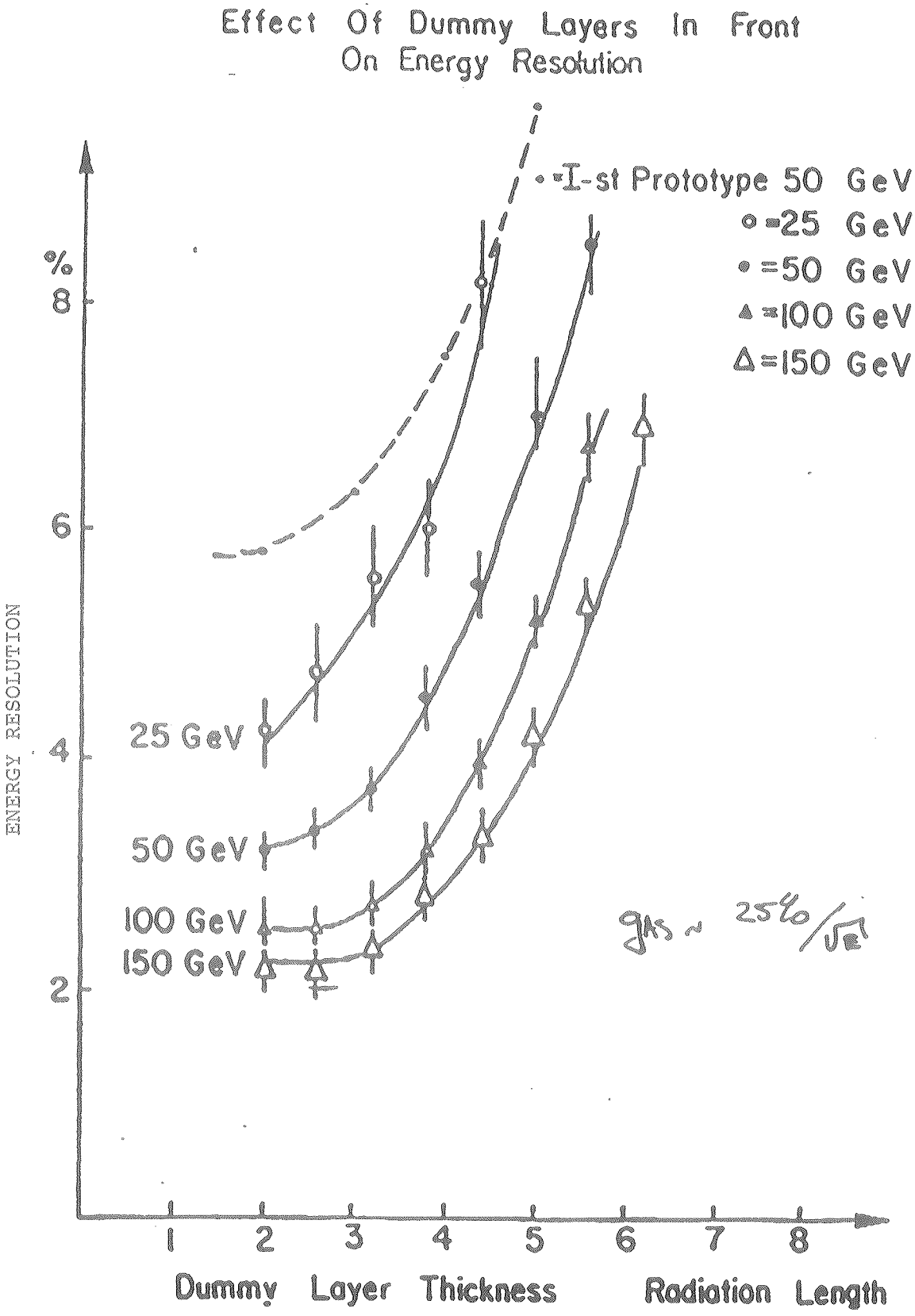
Effect Of Dummy Layers In Front
On Energy Resolution
•=1-st Prototype 50 GeV
o=25 GeV
•=50 GeV
▲=100 GeV
Δ=150 GeV
%
8
6
4
2
ENERGY RESOLUTION
25 GeV
50 GeV
100 GeV
150 GeV
σE/E ~ 25%/√E
1
2
3
4
5
6
7
8
Dummy Layer Thickness
Radiation Length

Figure 4-4.

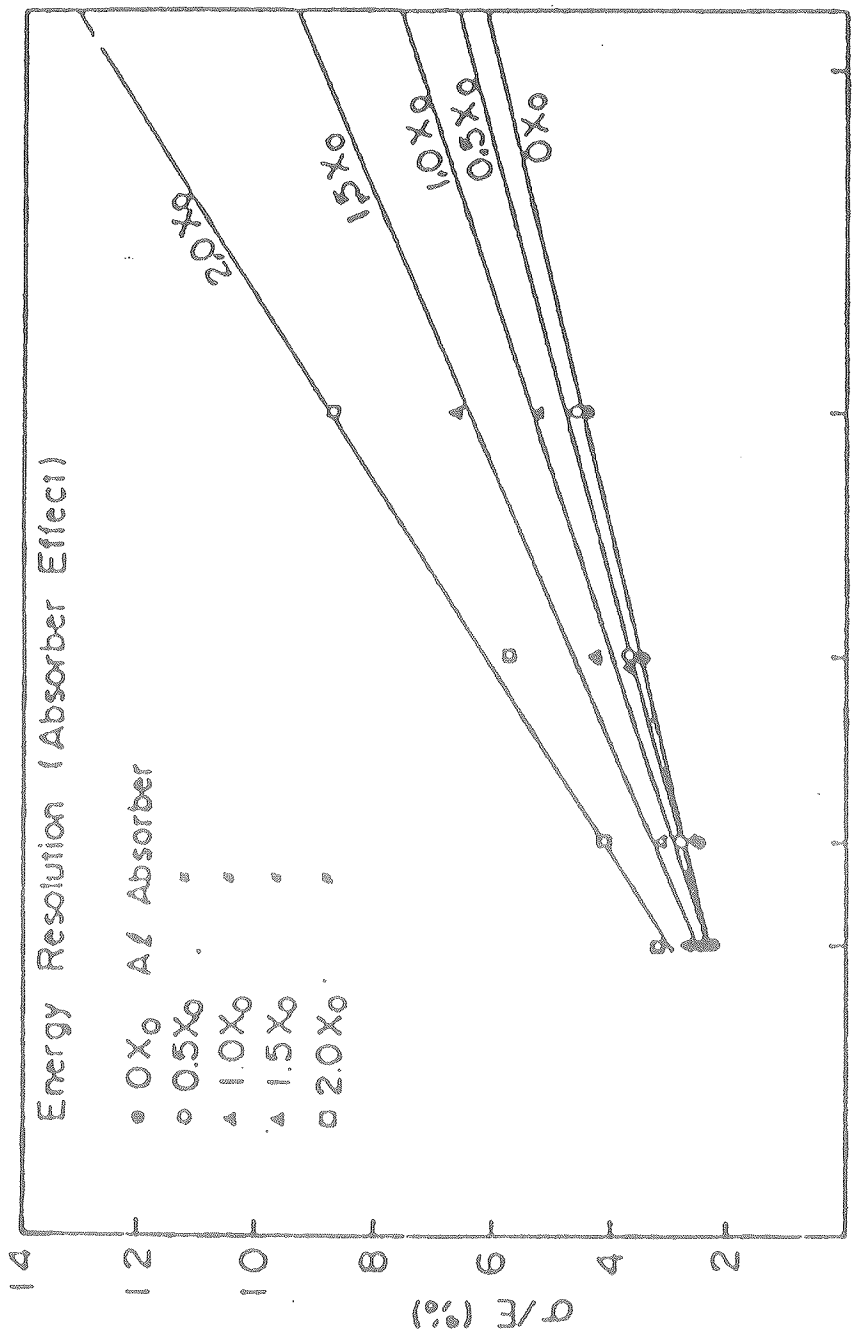
Energy Resolution (Absorber Effect)
• 0X₀ Al Absorber
○ 0.5X₀ "
▲ 1.0X₀ "
▲ 1.5X₀ "
□ 2.0X₀ "
2.0X₀
1.5X₀
1.0X₀
0.5X₀
0X₀
σ/E (%)
Energy (GeV)
14
12
10
8
6
4
2
16
10
4
2
1

Figure 4-5.

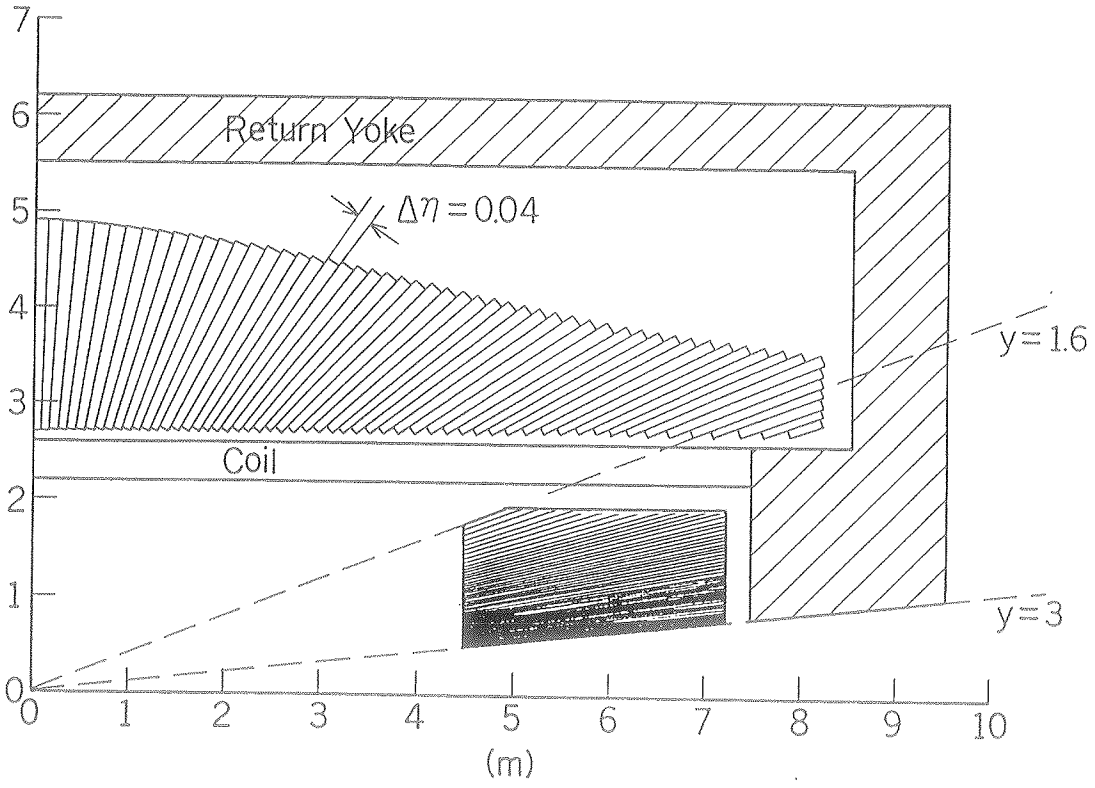
Return Yoke
Δη = 0.04
y = 1.6
Coil
y = 3
(m)

(a)

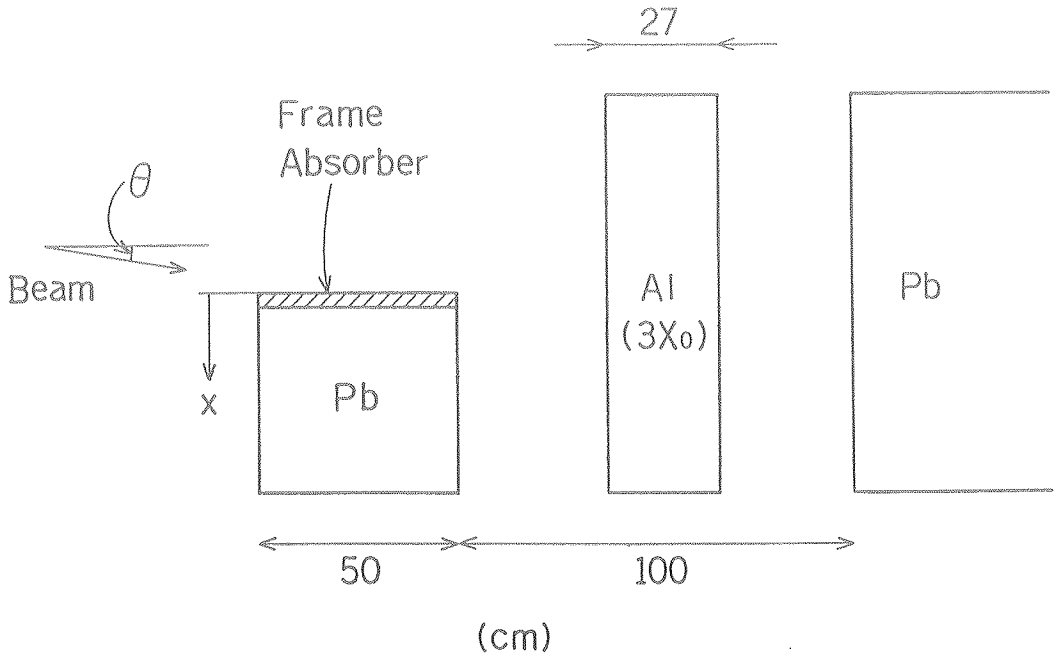
27
Frame
Absorber
θ
Beam
x
Pb
Al
(3X0)
Pb
50
100
(cm)

(b)

Figure 5-1.

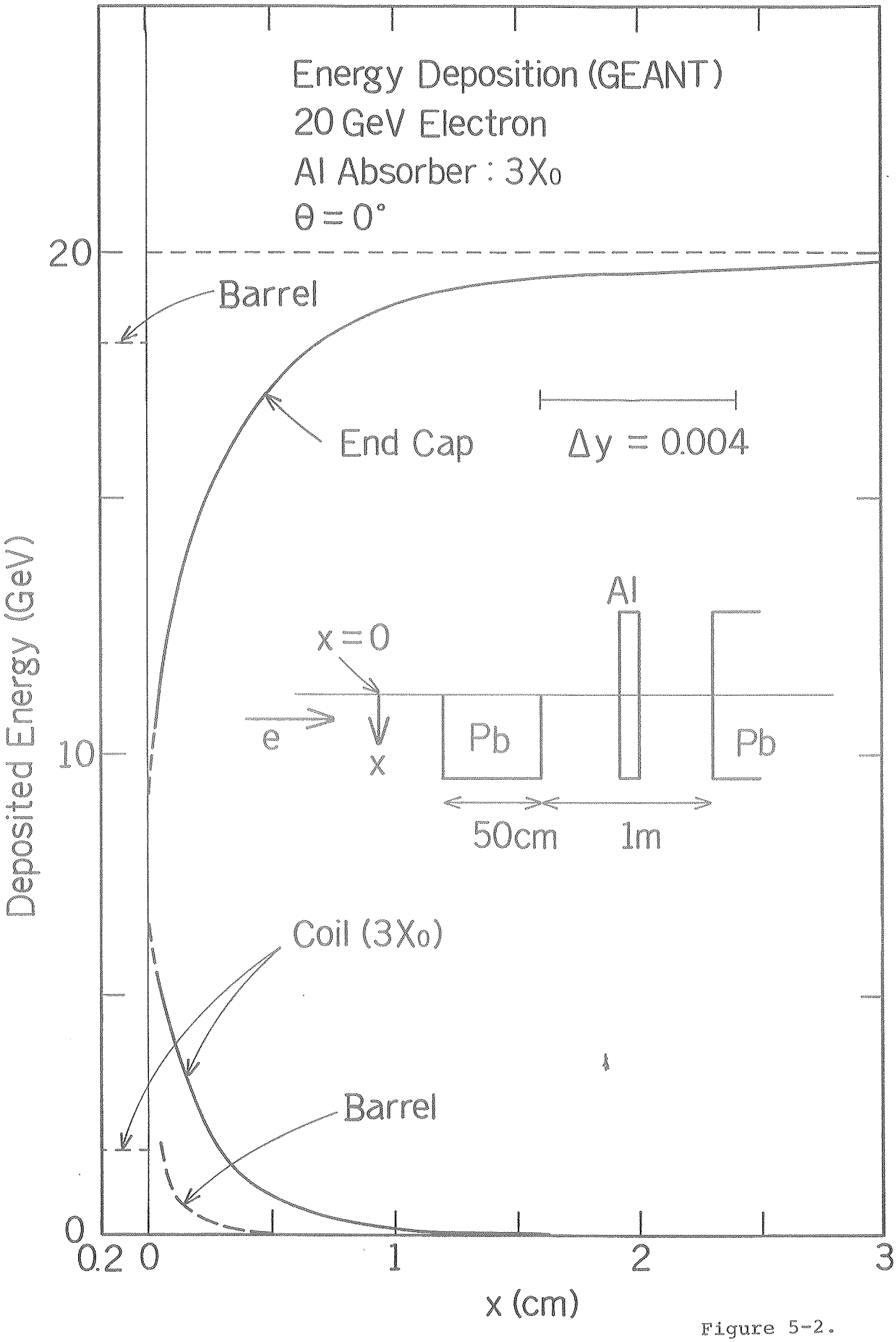
Energy Deposition (GEANT)
20 GeV Electron
Al Absorber : 3X0
θ = 0°
Barrel
End Cap
Δy = 0.004
Al
x = 0
e
x
Pb
Pb
50cm
1m
Coil (3X0)
Barrel
Deposited Energy (GeV)
20
10
0
0.2
0
1
2
3
x (cm)

Figure 5-2.

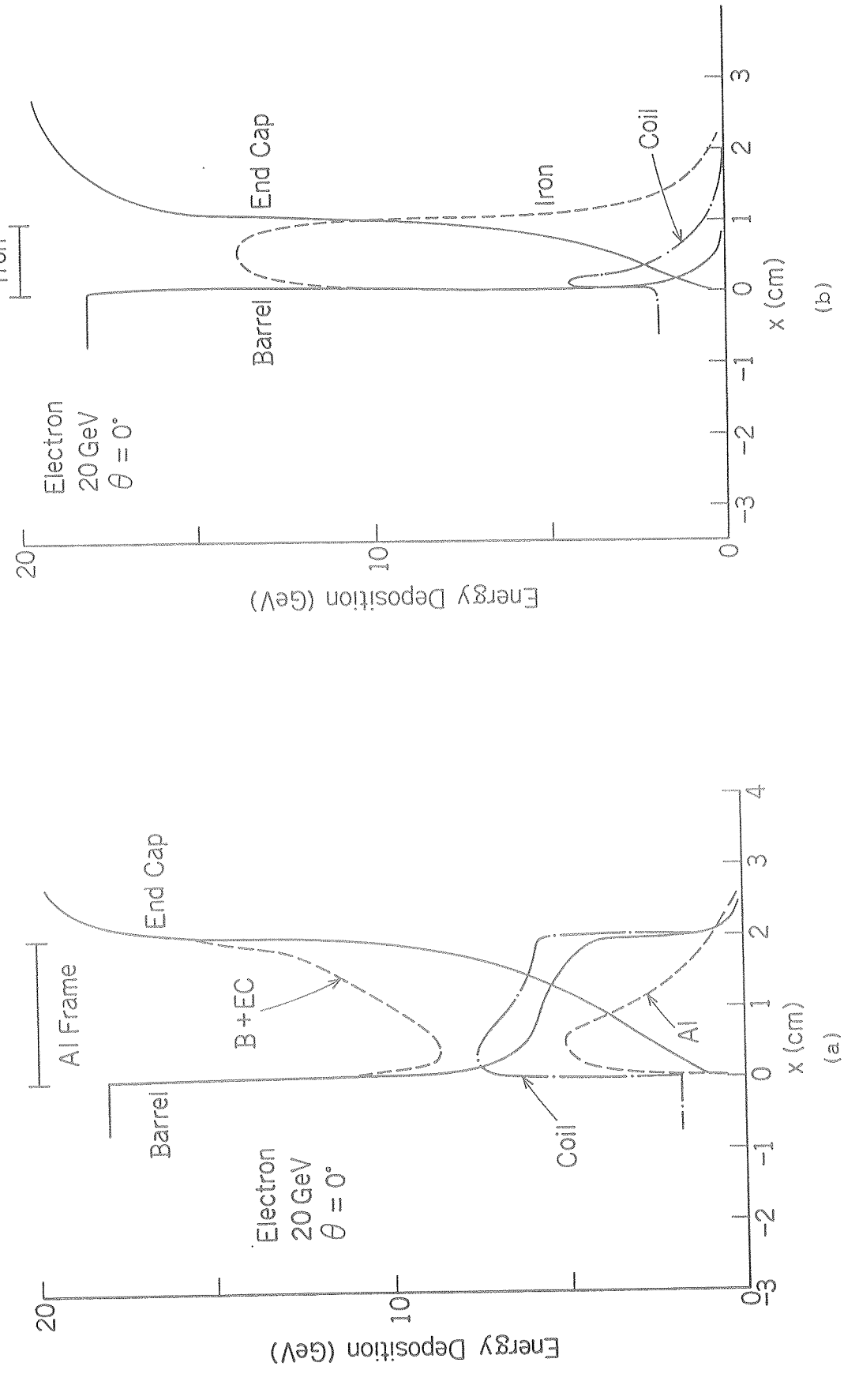
Energy Deposition (GeV)
20
10
0
Electron
20 GeV
θ = 0°
Iron
Barrel
End Cap
Iron
Coil
−3
−2
−1
0
1
2
3
x (cm)
(b)
Energy Deposition (GeV)
20
10
0
Electron
20 GeV
θ = 0°
Al Frame
Barrel
End Cap
B+EC
Coil
Al
−3
−2
−1
0
1
2
3
4
x (cm)
(a)

Figure 5-3.

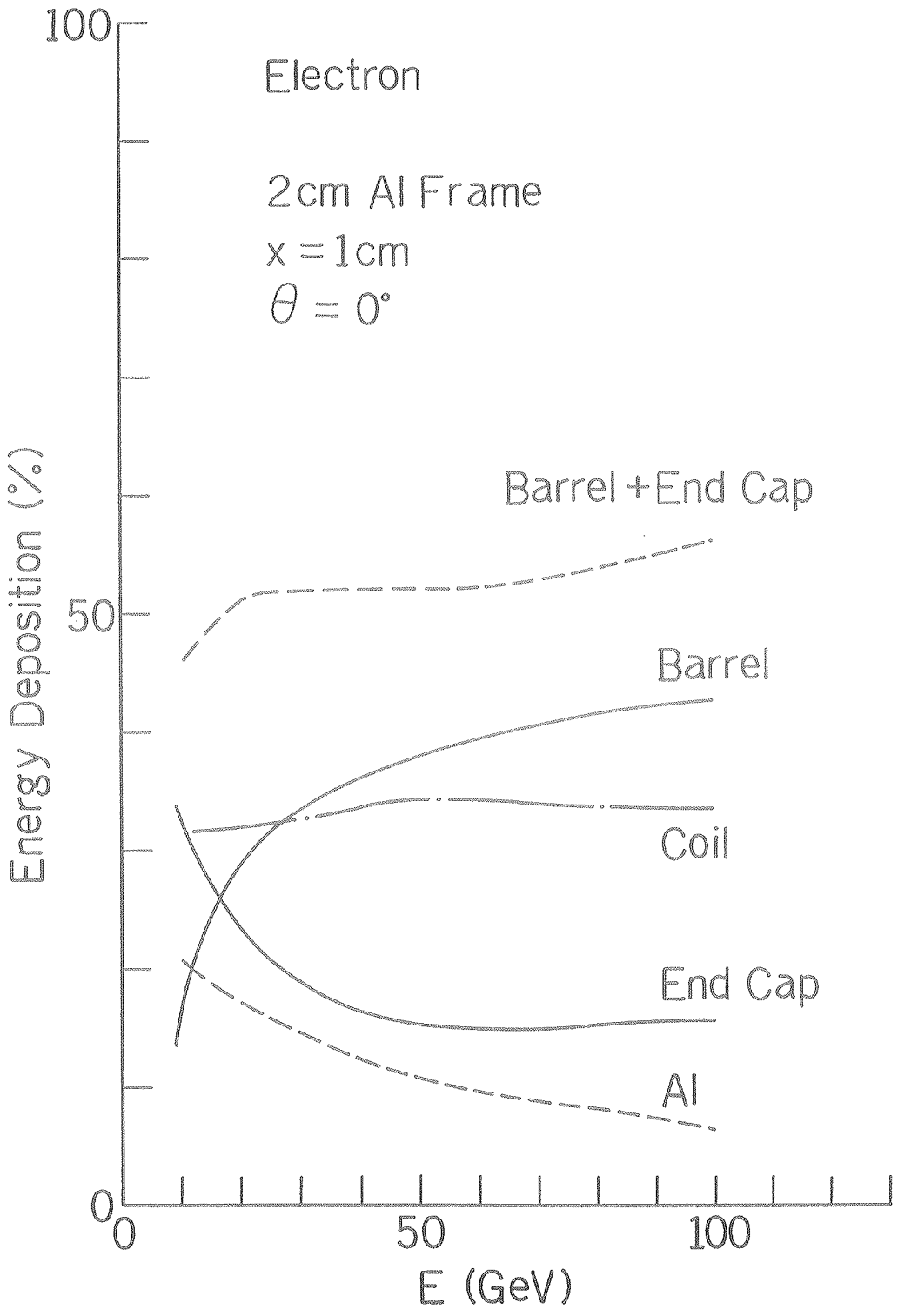
100
50
0
Energy Deposition (%)
Electron
2cm Al Frame
x = 1cm
θ = 0°
Barrel + End Cap
Barrel
Coil
End Cap
Al
0
50
100
E (GeV)

Figure 5-4.

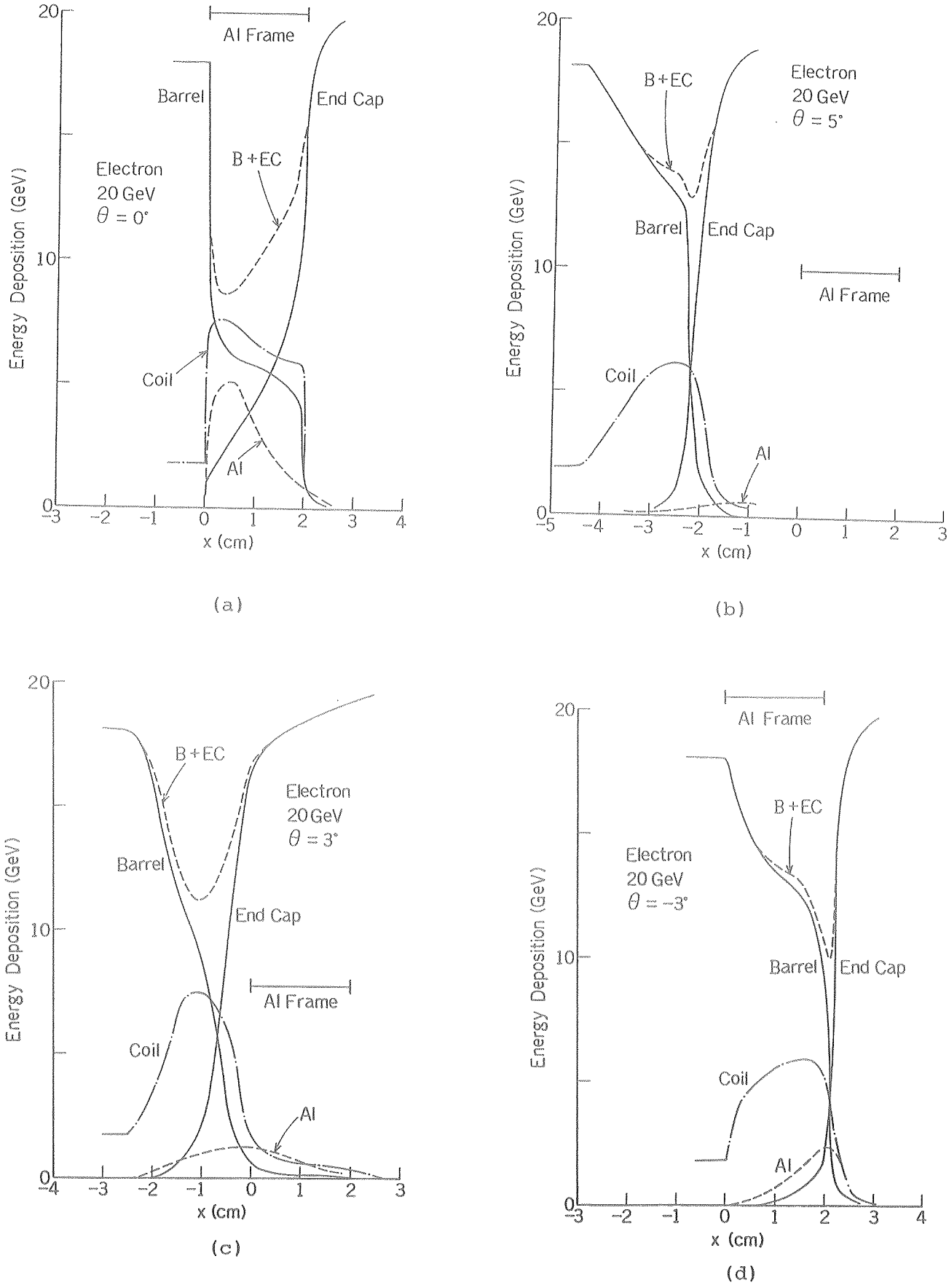
Al Frame
Barrel
End Cap
B+EC
Electron
20 GeV
θ = 0°
Coil
Al
Energy Deposition (GeV)
x (cm)
(a)
B+EC
Electron
20 GeV
θ = 5°
Barrel
End Cap
Al Frame
Coil
Al
Energy Deposition (GeV)
x (cm)
(b)
B+EC
Electron
20 GeV
θ = 3°
Barrel
End Cap
Al Frame
Coil
Al
Energy Deposition (GeV)
x (cm)
(c)
Al Frame
B+EC
Electron
20 GeV
θ = -3°
Barrel
End Cap
Coil
Al
Energy Deposition (GeV)
x (cm)
(d)

Figure 5-5.

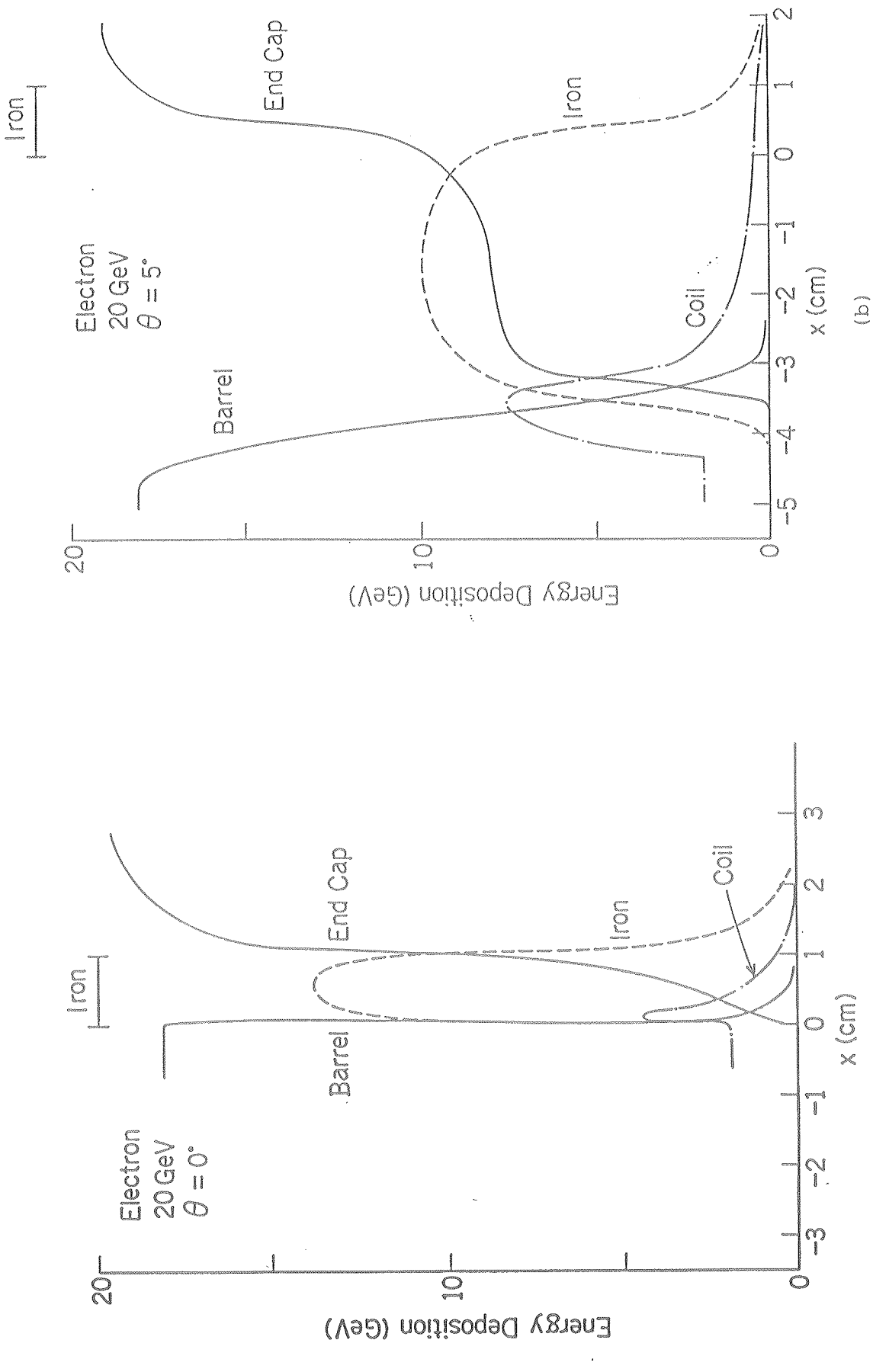
Energy Deposition (GeV)
20
10
0
Electron
20 GeV
θ = 0°
Iron
Barrel
End Cap
Iron
Coil
-3
-2
-1
0
1
2
3
x (cm)
(a)
Energy Deposition (GeV)
20
10
0
Electron
20 GeV
θ = 5°
Iron
Barrel
End Cap
Iron
Coil
-5
-4
-3
-2
-1
0
1
2
x (cm)
(b)

Figure 5-6.

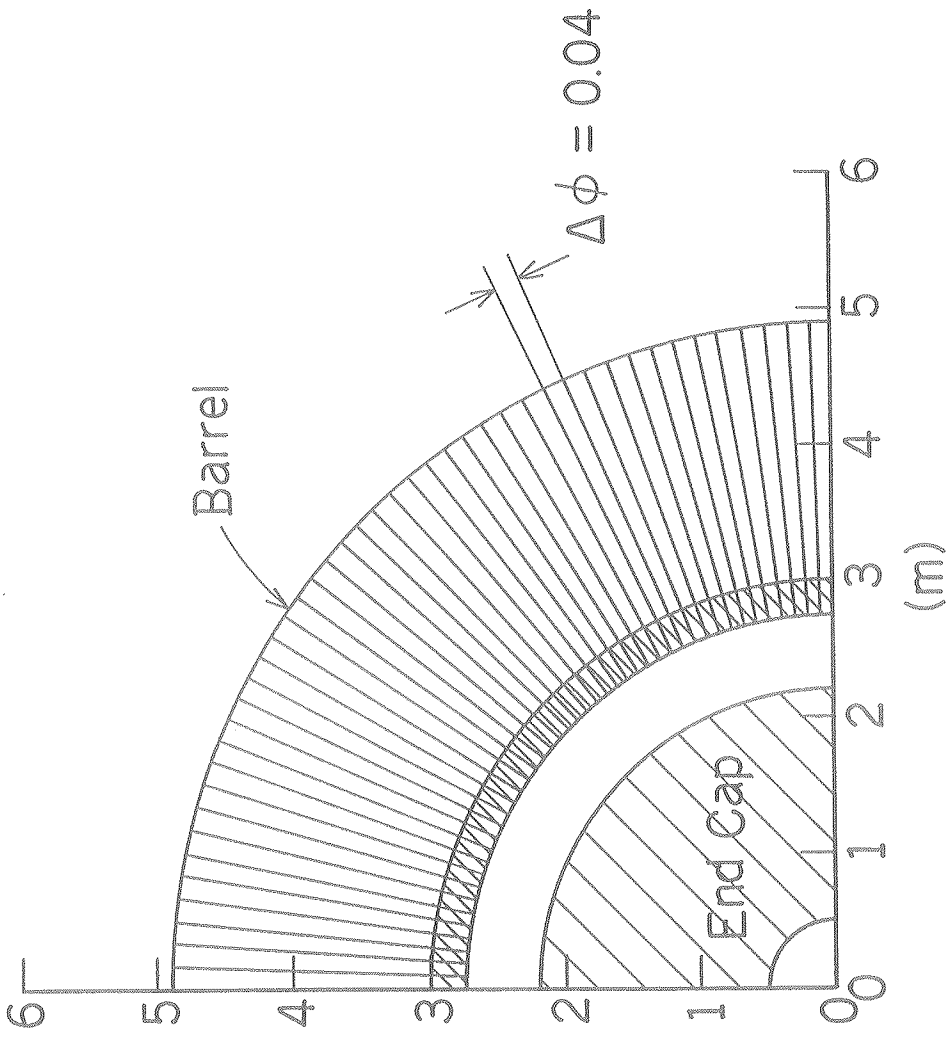


Figure 6-1.

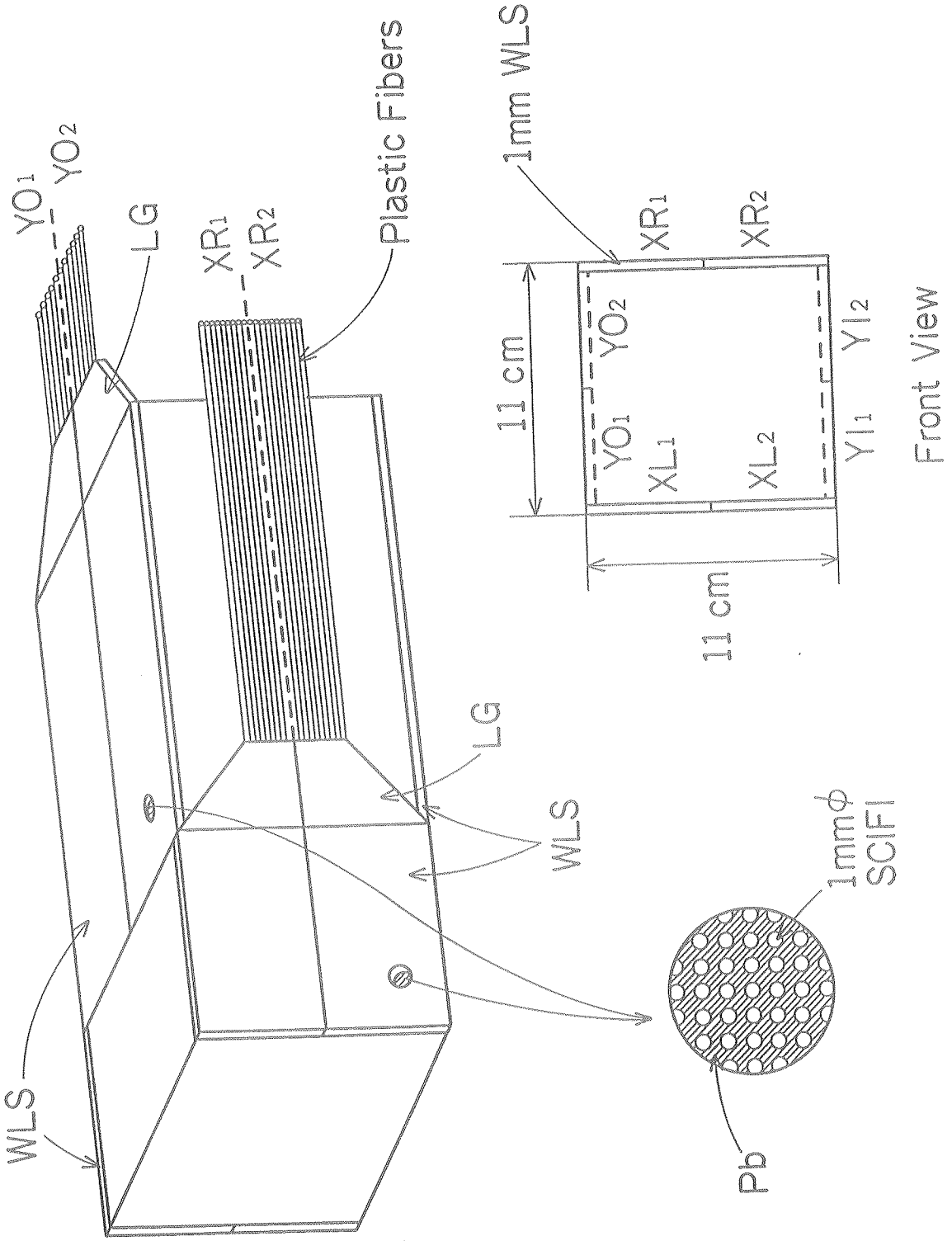
YO1
YO2
LG
XR1
XR2
Plastic Fibers
1mm WLS
11 cm
YO1
YO2
XL1
XL2
XR1
XR2
YI1
YI2
11 cm
Front View
WLS
LG
WLS
1mmϕ
SCIFI
Pb

Figure 6-2.

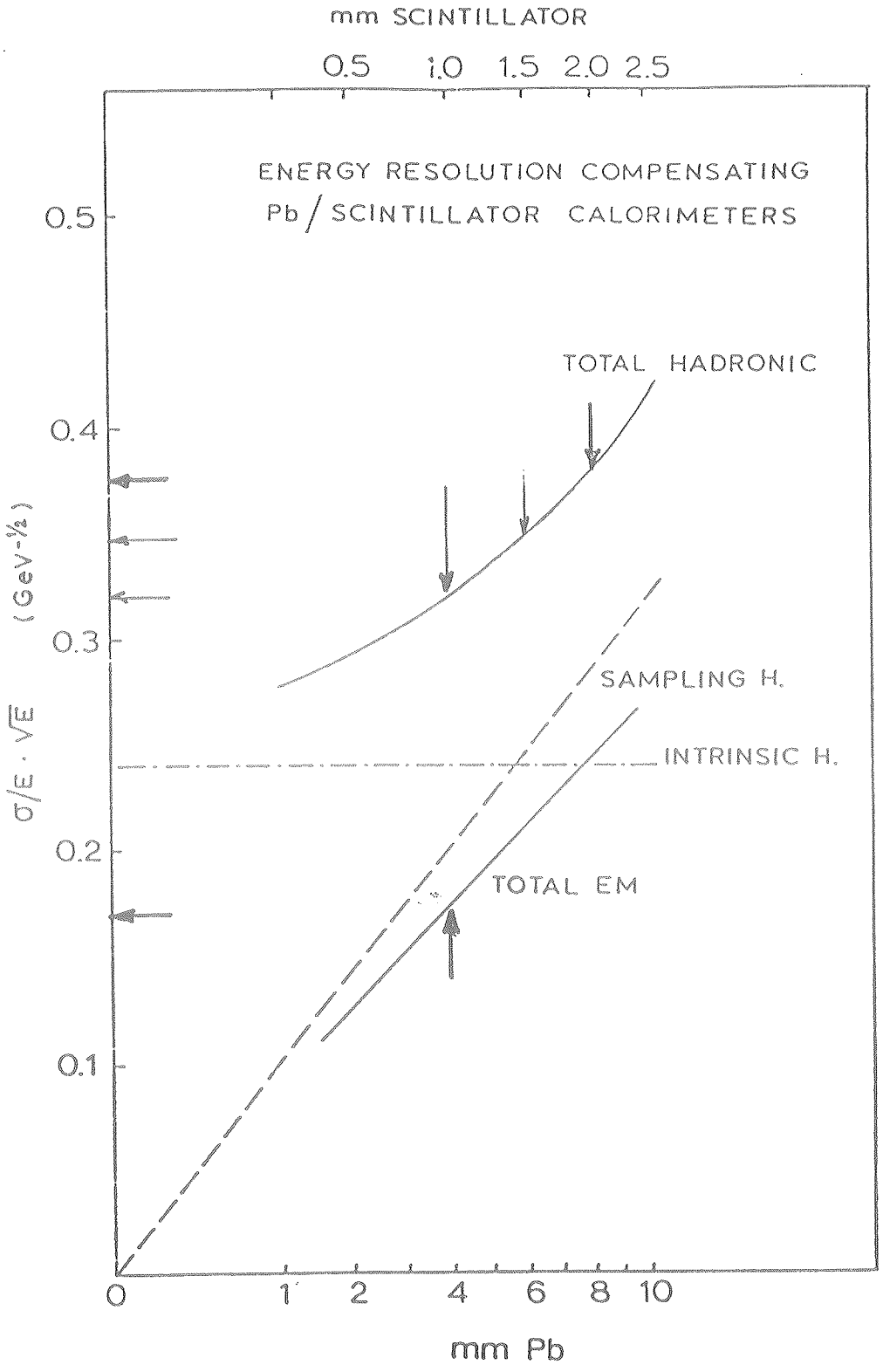
mm SCINTILLATOR
0.5 1.0 1.5 2.0 2.5
ENERGY RESOLUTION COMPENSATING
Pb / SCINTILLATOR CALORIMETERS
TOTAL HADRONIC
SAMPLING H.
INTRINSIC H.
TOTAL EM
σ/E · √E (GeV-½)
0.5
0.4
0.3
0.2
0.1
0 1 2 4 6 8 10
mm Pb

Figure 6-3.

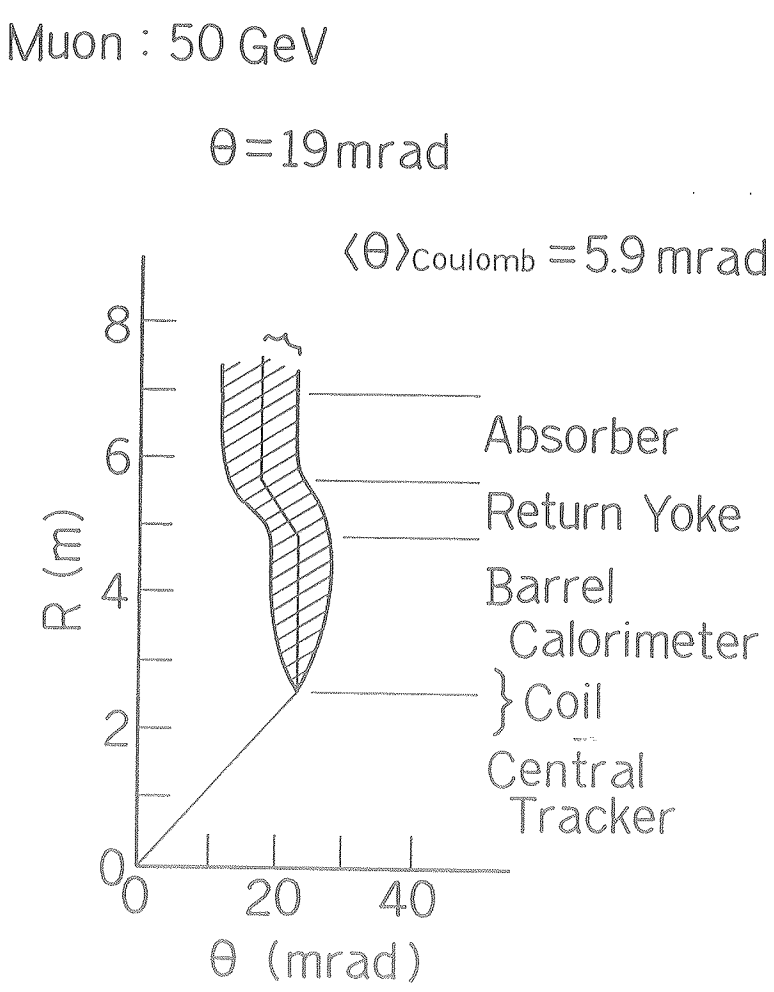
Muon : 50 GeV
θ=19mrad
⟨θ⟩Coulomb = 5.9 mrad
R (m)
8
6
4
2
0
0
20
40
θ (mrad)
Absorber
Return Yoke
Barrel
Calorimeter
} Coil
Central
Tracker

(a)

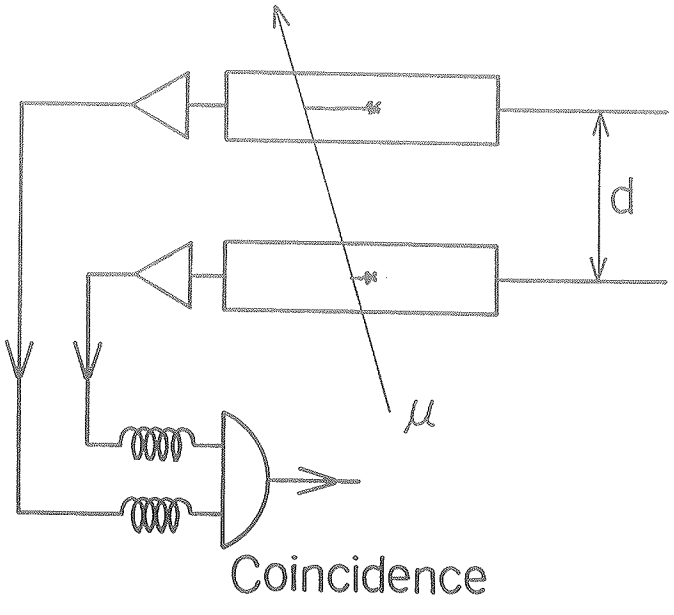
d
μ
Coincidence

(b)

Figure 7-1.